iScience

CellPress
OPEN ACCESS

Article

A Drosophila platform identifies a novel, personalized therapy for a patient with adenoid cystic carcinoma

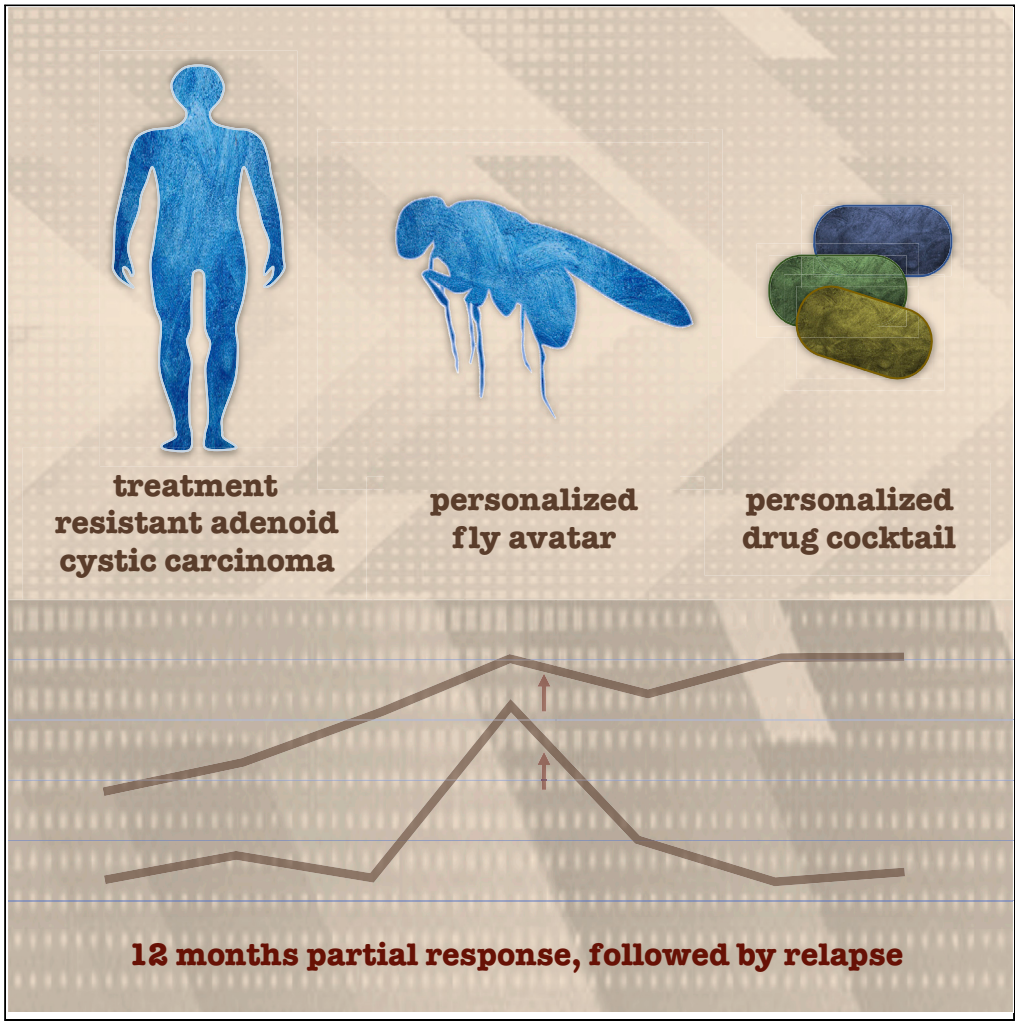

Erdem Bangi, Peter Smibert, Andrew V. Uzilov, ..., Eric E. Schadt, Marshall R. Posner, Ross L. Cagan

Ross.Cagan@glasgow.ac.uk

HIGHLIGHTS

Personalized therapy was developed for patient with Adenoid Cystic Carcinoma

Genomics analysis was leveraged to establish a Drosophila 'personalized patient avatar'

A robotics-based screen identified a novel three drug therapeutic cocktail

12 months response was followed by relapse and significant tumor genomic re-wiring

Bangi et al., iScience 24, 102212
March 19, 2021
https://doi.org/10.1016/j.isci.2021.102212

iScience

CellPress
OPEN ACCESS

Article

A Drosophila platform identifies a novel, personalized therapy for a patient with adenoid cystic carcinoma

Erdem Bangi,[1,8] Peter Smibert,[1,9] Andrew V. Uzilov,[3,4] Alexander G. Teague,[1] Sindhura Gopinath,[1,3] Yevgeniy Antipin,[3] Rong Chen,[3,4] Chana Hecht,[1] Nelson Gruszczynski,[1,10] Wesley J. Yon,[1] Denis Malyshev,[1,11] Denise Laspina,[1] Isaiah Selkridge,[2] Huan Wang,[4] Jorge Gomez,[2] John Mascarenhas,[2,7] Aye S. Moe,[3,4] Chun Yee Lau,[3,4,12] Patricia Taik,[3,4] Chetanya Pandya,[3,13] Max Sung,[2,7] Sara Kim,[5] Kendra Yum,[5] Robert Sebra,[3,4] Michael Donovan,[6,7] Krzysztof Misiukiewicz,[2,7] Celina Ang,[2,7] Eric E. Schadt,[3,4,7] Marshall R. Posner,[2,7] and Ross L. Cagan[1,7,14,15,*]

SUMMARY

Adenoid cystic carcinoma (ACC) is a rare cancer type that originates in the salivary glands. Tumors commonly invade along nerve tracks in the head and neck, making surgery challenging. Follow-up treatments for recurrence or metastasis including chemotherapy and targeted therapies have shown limited efficacy, emphasizing the need for new therapies. Here, we report a Drosophila-based therapeutic approach for a patient with advanced ACC disease. A patient-specific Drosophila transgenic line was developed to model the five major variants associated with the patient's disease. Robotics-based screening identified a three-drug cocktail—vorinostat, pindolol, tofacitinib—that rescued transgene-mediated lethality in the Drosophila patient-specific line. Patient treatment led to a sustained stabilization and a partial metabolic response of 12 months. Subsequent resistance was associated with new genomic amplifications and deletions. Given the lack of options for patients with ACC, our data suggest that this approach may prove useful for identifying novel therapeutic candidates.

INTRODUCTION

Adenoid cystic carcinoma (ACC) is a relatively rare neoplasm that metastasizes frequently and widely. ACC is the most common malignant tumor of the minor salivary glands and the second most common of the major salivary glands (Coca-Pelaz et al., 2015). Despite early dissemination, it is relatively slow growing. In the United States, approximately 20,000 patients are living with ACC in various stages of progression. One thousand two hundred new cases are reported annually; approximately 60% of those affected are women. On average, patients with ACC present in their 40s and therefore may live with their cancer for decades depending on the rate of progression, with consequent emotional and financial costs to family and society. The median survival is 85% at 5 years and 34% at 15 years, with lymphovascular invasion most associated with poor prognosis (Ouyang et al., 2017).

Patients with ACC have few therapeutic options. Treatment goals are limited and focused on achieving local or regional control through combinations of surgery, radiotherapy, and chemotherapy. Once disseminated or regionally recurrent, there are no effective therapies (Gatta et al., 2020). Chemotherapy and targeted therapies have proven poorly effective with arbitrary and transient responses (Tchekmedyian et al., 2019), while regional, focused therapies such as radiotherapy and surgery are used primarily to reduce symptoms (palliation) to address, *e.g.*, bronchial obstruction and symptomatic bone metastases.

Recent advances in genetic studies have pointed to further challenges: most ACC tumors contain the fusion myelobastosis viral oncogene homolog-nuclear factor 1B (MYB-NF1B (Persson et al., 2009; Andersson and Stenman, 2016) but also include multiple other cancer-associated gene mutations (Ho et al., 2013; Stephens et al., 2013; Ross et al., 2014; Mitani et al., 2016). MYB is a transcriptional activator with a C-terminal inhibitory domain (Sakura et al., 1989; Weston and Bishop, 1989; Dubendorff et al., 1992).

[1]Department of Cell, Development, and Regenerative Biology, Icahn School of Medicine at Mount Sinai, New York, NY 10029, USA

[2]Department of Medicine, Hematology and Medical Oncology, Icahn School of Medicine at Mount Sinai, New York, NY 10029, USA

[3]Department of Genetics and Genomic Sciences and Icahn Institute for Genomics and Multiscale Biology, Icahn School of Medicine at Mount Sinai, New York, NY 10029, USA

[4]Sema4, Stamford, CT 06902, USA

[5]Department of Pharmacy, The Mount Sinai Hospital, New York, NY 10029, USA

[6]Department of Pathology, Icahn School of Medicine at Mount Sinai, New York, NY 10029, USA

[7]Tisch Cancer Institute, Icahn School of Medicine at Mount Sinai, New York, NY 10029, USA

[8]Present address: Department of Biological Science, Florida State University, Tallahassee, FL 32306, USA

[9]Present address: Technology Innovation Lab, New York Genome Center, New York, NY 10013, USA

[10]Present address: Department of Otolaryngology-Head and Neck Surgery, University of Virginia, Charlottesville, VA 22903, USA

Continued

Most ACC tumors show activation of MYB through gene fusion of MYB with the transcription factor NFIB due to a 6;9 translocation (Persson et al., 2009; Andersson and Stenman, 2016) or, less often, by truncation or copy number gain (Persson et al., 2012). Fusion or truncation leads to loss of MYB's C-terminus, which is sufficient to generate a constitutively active MYB protein (Gonda et al., 1989); though unlikely (Persson et al., 2009), a function for the accompanying small (5 amino acids) C-terminal fragment of NFIB has not been ruled out. Most patients have additional mutations in other cancer-related genes such as activating mutations in the NOTCH1 and ERBB3 receptors and regulators of signal transduction and cell cycle (Ho et al., 2013; Stephens et al., 2013; Ross et al., 2014; Mitani et al., 2016). Our recent works, both basic and clinical (Bangi et al., 2016, 2019; Levine and Cagan, 2016; Levinson and Cagan, 2016), are consistent with a growing body of work demonstrating that tumor heterogeneity and genetic complexity can lead to drug resistance.

Recently, we described a personalized fly-to-bedside therapeutic discovery platform (Bangi et al., 2019) (Figure 1A). Modeling the disease of a patient with colorectal cancer in a personalized Drosophila transgenic model, we identified a novel two-drug cocktail that proved effective in both Drosophila and in the modeled patient. Building on this work, we present here a fly-to-bedside platform for ACC, a tumor that has resisted targeted therapies. We developed a personalized Drosophila line that targeted five genes altered in the patient's tumor. This "personalized avatar" exhibited aspects of transformation. We used this line as a screening tool to identify vorinostat-pindolol-tofacitinib as a three-drug cocktail that rescued transgene-mediated lethality in the fly avatar and led to stable disease and a metabolic response in the patient lasting for 12 months.

RESULTS

Clinical history

The patient presented with an extensive left-sided maxillary sinus ACC in February, 2013. At the time of presentation, the patient was a 54-year-old Caucasian male with no other significant medical problems. The tumor was found to invade the skin of the face, as well as the base of the skull on imaging. The patient underwent an extensive surgical resection (removal) of gross disease followed by reconstruction of the face and orbit. The tumor was staged as T3N0M0—indicating primarily localized disease—with perineural invasion and pathologically positive post-surgical margins.

The patient was treated with adjuvant proton beam radiation and weekly carboplatin and paclitaxel for 7 weeks for local regional control, completing therapy in June 2013. He underwent periodic surveillance imaging; enlarging pulmonary metastases were identified in March 2015. He was followed expectantly for symptoms and growth with periodic positron emission tomography and X-ray computed tomography (PET/CT) scans.

In January 2016, the patient was consented for participation in the "Personalized Cancer Therapy for Patients With Metastatic Medullary Thyroid or Metastatic Colon Cancer (NCT02363647)" protocol under a rare cancer cohort. A sample was obtained by excisional biopsy of a lung metastasis. This sample confirmed the diagnosis of ACC and was used for genetic analysis and confirmatory studies of genetic findings. Symptomatic bone metastases were identified in February 2017 by positron emission tomography (PET) imaging and magnetic resonance imaging. The patient received radiotherapy in March, May, and October, 2017 to thoracic bone metastases and a scapular metastasis, respectively. Imaging by PET/CT demonstrated increasing size and the number of bone and pulmonary metastases with increasing 2-deoxy-2-[^{18}F]fluoro-D-glucose (FDG) uptake during this period of time and prior to starting therapy.

The patient was consented for treatment on the protocol for a personalized treatment plan after reviewing results of drug screening on his tumor-matched fly avatar line. Assessment of his tumor by PET and CT imaging immediately prior to treatment demonstrated continued progression with growth of metastases, new metastases, and a rising standard uptake value (SUV) indicating increased metabolic activity by the tumor.

Genomic analysis and variant selection

Our overall approach is summarized in Figure 1A. The first step toward building a personalized Drosophila model for the patient was a comprehensive analysis of the tumor genomic landscape. Using a freshly frozen specimen from a lung metastasis obtained from a 2016 specimen prior to treatment on our study, we extracted DNA and RNA as well as DNA from a blood sample as matched control. For

[11]Present address: School of Medicine, St. George's University, St. George's, Grenada

[12]Present address: Department of Biomedical Informatics, Columbia University, New York, NY 10032, USA

[13]Present address: Bluebird Bio, Cambridge, MA 02142, USA

[14]Present address: Institute of Cancer Sciences-University of Glasgow, Glasgow, Scotland G61 1BD, UK

[15]Lead contact

*Correspondence: Ross.Cagan@glasgow.ac.uk

https://doi.org/10.1016/j.isci.2021.102212

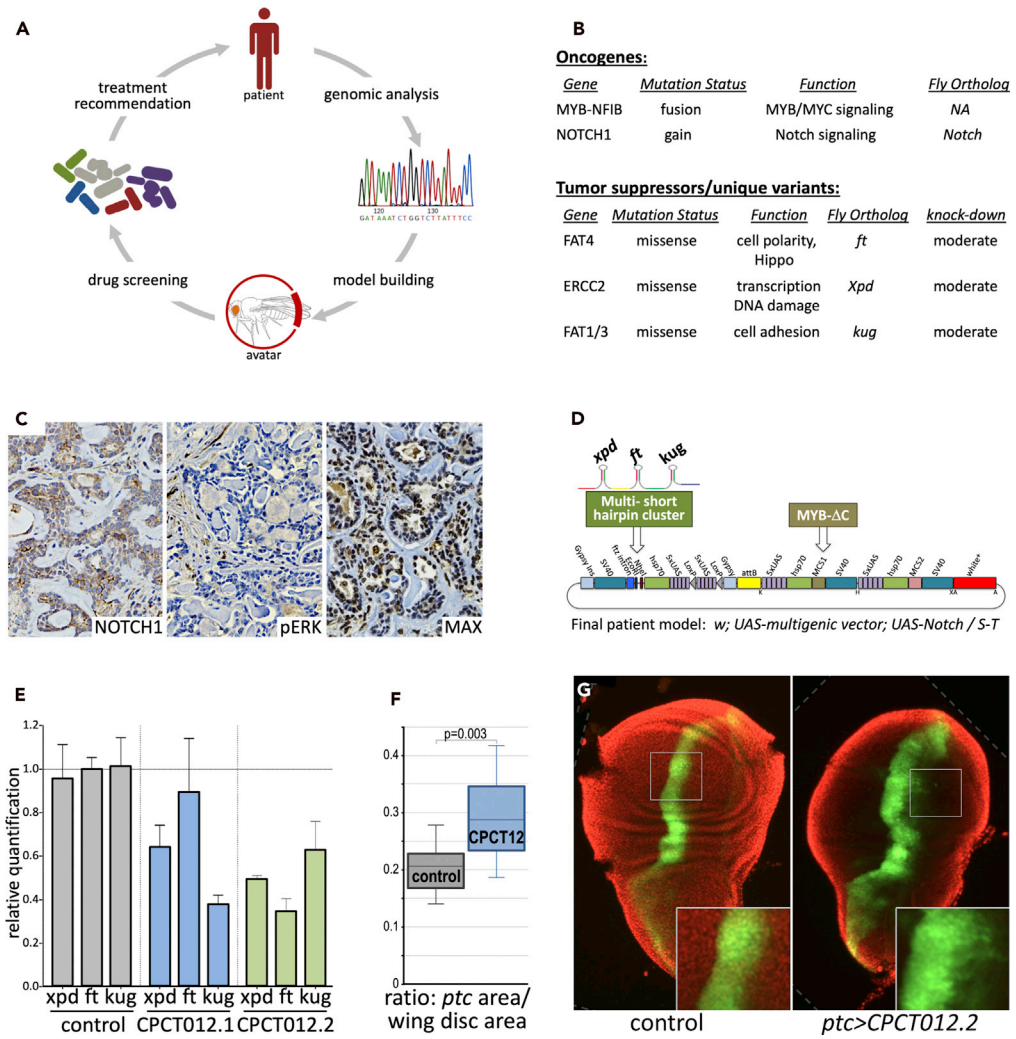

Figure 1. Developing a personalized Drosophila avatar screening platform

(A) Overview of personalized approach. Genomic analysis of the patient's tumor identified predicted tumor drivers used to develop a personalized fly avatar. Robotics-based drug screening identified a three-drug cocktail that was vetted for safety by a tumor board and internal review board.

(B) Prioritized oncogenes and tumor suppressors that emerged from our genomic analysis. *FAT4*, *ERCC2*, and *FAT1/FAT3* were heterozygous. See also supplemental figure, tables.

(C) Immunohistochemistry (brown) identified high levels of plasma membrane and nuclear NOTCH1, indicating elevated NOTCH1 protein and activity in patient tumor sections obtained prior to treatment. Similar immunohistochemical assays failed to validate elevated MAP2K2 activity (pERK) or loss of MAX, and neither were included in the final avatar model.

(D) Schematic of transformation vector used to target 4 of 5 cancer genes to different Drosophila tissues. Inducible Notch overexpression (*UAS-Notch*) was introduced by standard genetic crosses.

(E) Small hairpins targeting *xpd*, *ft*, and *kug* in CPCT012.2 led to a ~50% reduction in expression as assessed with qPCR. We used this line as the best model of heterozygosity.

(F) Quantifying results of directing *ptc* > *CPCT012* expression on the wing's *ptc* domain, which led to expansion of the domain including a loss of the sharp boundary. Results are represented as the ratio of the *ptc* domain area to total wing disc area.

(G) Example of *ptc* > *CPCT012*-mediated expansion. The *ptc* domain was visualized with an included *UAS-GFP* marker (green). Insets highlight expansion; dotted lines indicate added black background to square images. Error bars represent standard error of the mean.

genomic analysis of small molecular variants and copy number variants (CNVs), we performed whole-exome sequencing (WES) using tumor and matched normal blood DNA as well as RNA sequencing (RNA-seq).

The ACC genomic landscape is typically diverse and includes many low frequency drivers (Ho et al., 2013; Rettig et al., 2016). As a result, identifying driver alterations and building representative models are challenging. Commonly altered pathways in ACC tumors include overactivation of the MYB/MYC, NOTCH and FGF/IGF/PI3K pathways, as well as alterations in DNA damage repair and chromatin remodeling pathway components (Ho et al., 2013; Rettig et al., 2016). WES of our patient's tumor DNA from the 2016 specimen—obtained prior to treatment—identified 11 nonsynonymous somatic mutations (SNVs/indels) with allelic fraction (AF) $\geq$0.05 (Table S1), none of which were in genes previously associated with ACC. Most were novel, functionally uncharacterized variants in genes that were not previously associated with cancer.

In the absence of experimental data, we utilized functional prediction algorithms to determine the likelihood that each variant was deleterious (*i.e.* had a negative impact on protein function) (Kircher et al., 2014; Liu et al., 2016). Most WES variants found in the patient's tumor were predicted to be benign by two different functional prediction tools and were eliminated. Finally, we discarded variants that were not detected by RNA-seq, suggesting that they were either false positives or they were not expressed in the tumor. At the end of our analysis, we concluded that none of the somatic variants were appropriate for model building.

In addition to somatic mutations, we also identified 935 rare germline variants in the patient's non-tumor (*i.e.* blood) DNA. Given this large number, we focused our analysis on variants in genes previously associated with cancer, as well as those encoding components of cancer relevant pathways and cellular processes. Of these, we found that heterozygous missense mutations in four genes—*FAT4*, *FAT1*, *FAT3*, and *ERCC2*—were predicted to be deleterious and also detected by tumor RNA sequence data, indicating that the mutant alleles were expressed in the tumor. These were selected for the fly model (Figure 1B).

NOTCH1 is a component of the NOTCH signaling pathway frequently activated in ACC (Ho et al., 2013). Although copy number analysis was inconclusive, elevated NOTCH1 protein in the tumor specimen was established by immunohistochemistry (Figure 1C). Two other potential variants, MAP2K2 (predicted gain) and MAX (predicted loss), were rejected by similar immunohistochemical criteria (Figure 1C). In addition, RNA-seq data revealed a t(6;9) (q22-23;p23-24) MYB-NFIB fusion event in our patient's tumor, a commonly observed cancer driver in patients with ACC (Ho et al., 2019). In our patient's tumor, the fusion event resulted in an out-of-frame transcript encoding a truncated, constitutively active MYB protein that lacked the C-terminal cytoplasmic domain required to regulate its activity (West et al., 2011). NOTCH1 and truncated MYB—which together define a common subtype of adenoid cystic carcinoma (Ho et al., 2019)—were also selected for the fly model, bringing the final number of modeled cancer drivers to six patient variants modeled by five targeted fly genes (Figure 1B).

Model building and validation

To create a patient-specific model that represents the six alterations identified in our genomic analysis (Figure 1B), we utilized a multigenic vector platform that we tailored for this purpose (Bangi et al., 2019). This vector carries three different multiple cloning sites, each flanked by promoter and transcription terminator sequences: two are designed for protein expression to model oncogenes, and one is reserved for short hairpin-mediated knockdown of Drosophila tumor suppressor orthologs (Figure 1D). Transgenes were cloned downstream of a GAL4-inducible *UAS* promoter, a well-established ectopic expression system in Drosophila that allows both spatial and temporal control of transgene expression (Brand and Perrimon, 1993). Transgene expression was targeted by crossing the patient-specific transgenic line to transgenic fly lines that express GAL4 in specific tissues, such as *ptc-GAL4*. The result was a "*ptc > CPCT012.2*" transgenic fly line that expressed the transgenes—targeting five fly orthologs of six patient variants—in discrete regions across the developing fly.

Previous work found that expressing full-length c-MYB in Drosophila can disrupt developing tissues including aspects of the cell cycle (Lipsick et al., 2001; Fitzpatrick et al., 2002; Davidson et al., 2005). To model the *MYB-NFIB* fusion, we generated a truncated *MYB* construct that represents the product of the translocation event (*MYBΔC*). *NOTCH1* copy gain was modeled by overexpressing a wild-type Drosophila Notch cDNA. Heterozygous missense variants in *FAT4*, *FAT1/3*, and *ERCC2* were modeled by targeting their Drosophila orthologs using short hairpins designed to achieve moderate knockdown (to model the heterozygous nature of each variant). Individual hairpins targeting each gene were selected using previously reported protocols (Vert et al., 2006; Ni et al., 2011) and stitched together as a synthetic

multi-hairpin cluster using our microRNA-inspired design (Bangi et al., 2019). As hairpin selection relies on algorithms to predict efficacy (Vert et al., 2006; Ni et al., 2011), we generated two hairpin clusters targeting the same three Drosophila genes with different hairpins—*12.1* and *12.2*—to increase the likelihood of success.

To build the patient-specific multigenic vector, the *MYBΔC* coding sequence and the hairpin cluster were cloned into their respective multiple cloning sites, each downstream of their own inducible UAS promoter (Figure 1D). We generated two different versions of the patient model: CPCT012.1 and CPCT012.2. Both versions carried the same MYBΔC transgene but a different hairpin cluster designed to reduce expression of Drosophila orthologs of *FAT4*, *FAT1/3*, and *ERCC2*. We established two transgenic lines using a site-specific chromosomal integration method mediated by standard ϕC31-based integration (Bischof et al., 2007). Once transgenic lines were established, an existing *Notch* transgenic construct that expresses the full-length Drosophila Notch protein under *UAS* control (Matsuno et al., 2002) was introduced into each line by standard genetic crosses.

Once the two final patient models were established, we ubiquitously expressed each multigenic construct (*tub > CPCT012*) in developing larvae to determine whether the hairpin clusters we generated were effective. Quantitative polymerase chain reaction (qPCR) analysis indicated that the short hairpin cluster in CPCT012.2 was effective in moderately reducing expression of all three genes, our goal for modeling heterozygous variants; CPCT012.1 did not show significant knockdown of the Drosophila FAT4 ortholog *ft* (Figure 1E). We therefore focused on the CPT012.2 patient-specific transgenic line for further characterization.

To further validate the CPCT012.2 line, we used *ptc-GAL4* to direct transgene expression within several tissues including a discrete stripe of expression at the developing wing epithelium's anterior/posterior boundary (Figures 1F and 1G). In previous work, expressing oncogenes with the *ptc-GAL4* driver led to expansion of the *ptc* domain in the developing wing, reflecting overproliferation (Vidal et al., 2006; Vidal et al., 2007; Levinson and Cagan, 2016; Sonoshita et al., 2018). Consistent with promoting at least one aspect of transformation, expressing the transgenes at the larval wing boundary (*ptc > CPCT012.2*) led to expansion of the *ptc* domain (Figures 1F and 1G). We concluded this model could prove useful as an accessible whole animal platform to screen for candidate therapeutics.

Drug screening

Rescue from lethality is a useful primary readout for whole animal drug screens, providing rapid, quantitative data (Rudrapatna et al., 2014; Levine and Cagan, 2016; Bangi et al., 2019). We have successfully used *ptc-gal4* in previous genetic and drug screens of Drosophila cancer models (Dar et al., 2012; Sonoshita et al., 2018). We therefore calibrated *ptc > CPCT012.2* flies for lethality, using temperature to alter GAL4 activity to a level of near-complete animal lethality.

We previously found that most drugs are not effective as single agents against genetically complex cancer models (Bangi et al., 2019). We therefore used an iterative screening process to progressively identify drug combinations (Figure 2A). We first screened a custom-built 'Focused FDA-Approved Library' of 122 drugs/drug combinations enriched for cancer relevant activities. We identified and confirmed two hits with weak efficacy: the chemotherapy drug docetaxel is an anti-microtubule agent; the JAK inhibitor tofacitinib (Changelian et al., 2003; Vyas et al., 2013) is FDA approved for rheumatoid arthritis, ulcerative colitis, and psoriatic arthritis (Figures 2A and 2B). The patient was previously treated with the anti-microtubule agent paclitaxel as part of a combination therapy with carboplatin, and we therefore did not pursue docetaxel further.

Tofacitinib is a promising candidate for combination screens. Its target pathway, JAK/STAT signaling, can be activated by NOTCH in cancer cells (Jin et al., 2013), which was elevated in the patient's tumor. Re-screening the Focused Library in the presence of low dose tofacitinib (see methods) identified the DNA synthesis inhibitor and FDA-approved chemotherapy agent gemcitabine as an effective partner for tofacitinib (Figures 2A and 2C). We also screened a commercially available "FDA-Approved Drug Library" of 1280 drugs approved for all indications, again in combination with low dose tofacitinib. These combination screens identified several tofacitinib drug combinations with low efficacy. We then tested all confirmed hits in double and triple combinations (Figure 2A). From these screens, a three-drug cocktail emerged

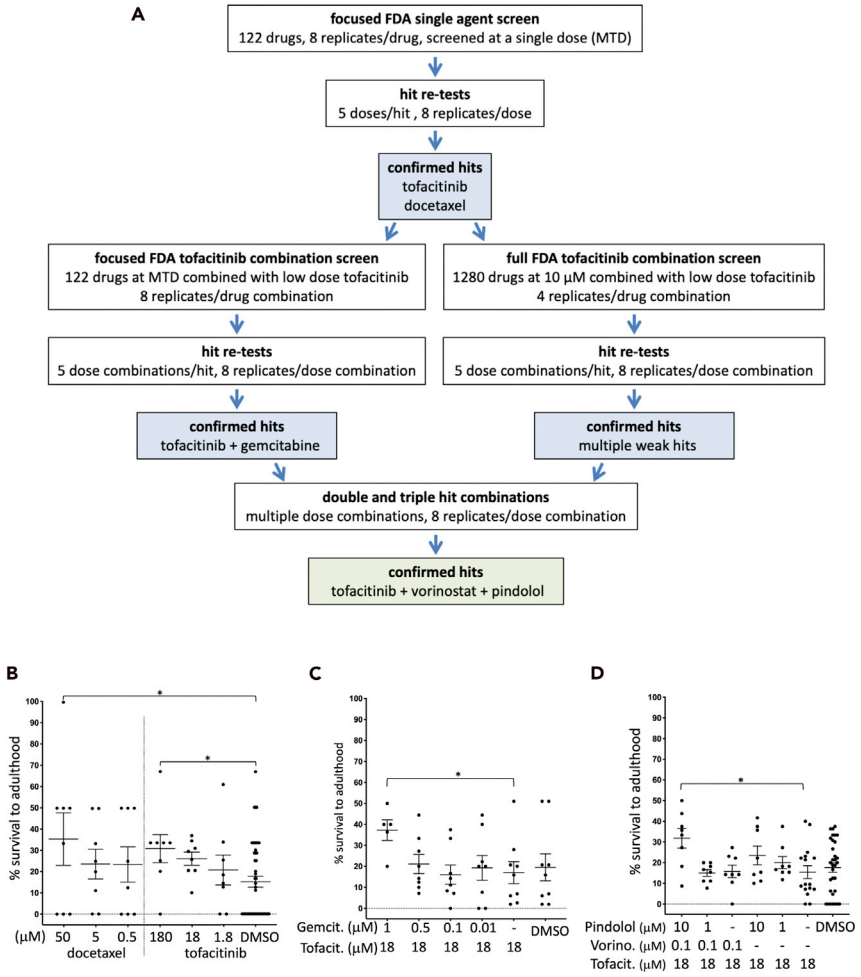

Figure 2. Screen for candidate combinations of FDA-approved drugs

(A) Flowchart of multi-step drug screen. An initial screen of the Focused FDA Library yielded tofacitinib and docetaxel as weak single agent hits. Subsequent screens identified tofacitinib, vorinostat, and pindolol as an effective 3-drug combination.

(B) Data demonstrating initial rescue by docetaxel and tofacitinib as single agents.

(C) Data demonstrating CPCT012 rescue to adulthood by gemcitabine plus tofacitinib, an effective two-drug combination. Tofacitinib was used at a dose below that required for significant rescue.

(D) Data demonstrating CPCT012 rescue to adulthood by tofacitinib, vorinostat, and pindolol. The 3-drug combination proved the most effective at rescuing CPCT012 to adulthood. Asterisks (*) in panels (B–D) indicate $p < 0.05$ as assessed by Student's t-test. Error bars represent standard error of the mean.

(Figure 2D): tofacitinib, vorinostat (histone deacetylase inhibitor, anti-cancer agent), and pindolol (a non-selective beta blocker used to treat high blood pressure).

Each drug identified in our screens has been reported to have targets or anti-tumor effects that could be relevant to our patient tumor's genomic profile. Tofacitinib is an inhibitor of JAK/STAT signaling (Vyas et al., 2013), a cancer-relevant pathway that can be activated downstream of Notch signaling in tumor cells (Jin et al., 2013). Gemcitabine is a nucleoside analog that interferes with DNA synthesis (Plunkett et al., 1995) and is approved for treatment of multiple cancer types. The histone deacetylase (HDAC) inhibitor vorinostat may be particularly relevant for treatment of ACC, as deregulation of chromatin remodeling is observed in about 35% of sequenced tumors (Duvic and Vu, 2007; Marks and Breslow, 2007; Ho et al., 2013). A mechanism of action clearly relevant to cancer has not been reported for pindolol. However, there is some evidence suggesting that inhibition of β-adrenergic signaling by beta blockers can have anti-tumor effects, including inhibition of tumor cell proliferation, migration, invasion, angiogenesis, and metastases

(Creed et al., 2015; Partecke et al., 2016; Wrobel et al., 2016). A positive correlation between beta blocker use and cancer-specific survival has been documented (Na et al., 2018), although no causal relationship between the two has been reported.

Our findings were reviewed by a multidisciplinary tumor board that included pharmacists and oncologists with expertise in clinical trial design and dosing. The tumor board raised some concerns regarding myelosuppression, the major dose limiting toxicity associated with gemcitabine. Given the concerns with gemcitabine and both the clinical relevance of the signaling nodes targeted by the triple drug combination and their particular importance for this patient's tumor genome landscape, the tumor board unanimously selected the tofacitinib/vorinostat/pindolol triple combination as the first line recommendation for the patient.

Patient treatment

The patient initiated treatment orally with 400 mg of vorinostat daily (2800 mg/week), 10 mg of tofacitinib daily, and 10 mg of pindolol daily beginning on 4/19/18. At four weeks, grade 1 thrombocytopenia, creatinine elevation, and folliculitis were observed likely due to vorinostat; minor fatigue was reported likely due to pindolol. All the drugs were held and then restarted 10 days later with 400 mg of vorinostat reduced to five days per week (2000 mg/week). Recurrent rash, thrombocytopenia, and creatinine elevation developed after restarting vorinostat, which resolved after halting and then restarting vorinostat with a further dose reduction to 300 mg four days per week (1200 mg/week) after which creatine and platelet counts remained within normal limits.

In response to treatment, the patient exhibited documented stable disease (Figure 3) with no new bone lesions and mild regression of lung lesions. Quantitative imaging of a FDG tracer with PET/CT scans was used to measure relative glucose uptake by the tumor. Cumulative FDG data over time indicated a significant reduction (49%) in SUV in pulmonary and bone metastases (Figure 3), indicating a significant metabolic response.

The patient continued on therapy until 4/19/2019 (12 months), when he exhibited documented progression by progression by response evaluation criteria in solid tumors (RECIST), version 1.1, criteria. He had subsequent palliative surgery, chemotherapy, and radiation for further rapid progression. The patient passed away on 3/17/2020.

Post-treatment analysis

To better understand the nature of the emergent resistance at 12 months, we obtained two additional biopsy samples from the patient shortly after he stopped receiving the drug cocktail treatment in April 2019. Similar to the original sample, WES was performed on both biopsies: two specimens were obtained from the same formalin-fixed paraffin-embedded (FFPE) tumor block in June 2019 biopsy; a bone biopsy specimen was obtained in October 2019. The somatic non-synonymous small molecular variants with AF $\geq$0.05 and CNVs from the post-treatment 2019 specimens were compared to the original pre-treatment 2016 specimen. We observed significant genomic differences (Figure 4).

A small number of somatic variants were common to all 2019 specimens but not the 2016 specimen (Figure 4A and Table S1). These included variants in genes encoding ANKAR, ANXA8L2, CNTRL, EP300, GEMIN5, which are therefore candidates to play a role in the resistance that emerged during treatment. Somatic copy number variants (sCNVs), identified by saasCNV (Zhang and Hao, 2015), found that all three 2019 specimens had a significantly larger number of sCNVs than the original 2016 sample, which had relatively few sCNVs (Figure 4B). Loss of a large segment on chromosome 14 in the original specimen was the sole sCNV retained in 2019 specimens; in contrast, *e.g.*, an aneuploid gain of chromosome 19 from the original specimen was lost in all 2019 specimens, suggesting the aneuploid gain was contained within a subclonal alteration that was selected against as the patient's disease advanced. GATK4 sCNV was used to confirm the sCNV calling in the 2019 specimens (Figure S1, Tables S2 and S3; see also methods); the sCNV profiles between the two callers largely agreed with each other.

Finally, to further identify driver genes responsible for emergent resistance, annotated tumor suppressor genes by Catalogue of Somatic Mutations in Cancer (COSMIC) Cancer Gene Census (Sondka et al., 2018) were checked against the biallelic inactivated genes (defined by the intersection between loss sCNVs

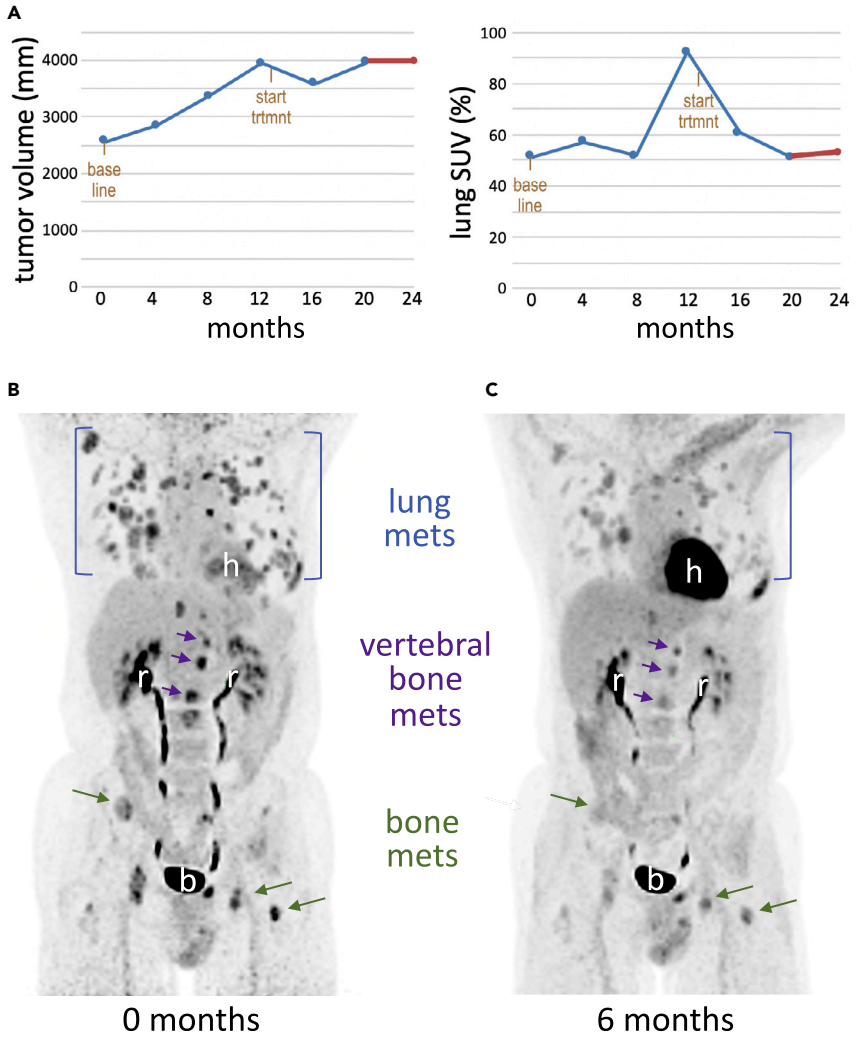

Figure 3. Body PET scans from baseline and after 6 months of treatment

(A) Prior to the start of treatment, tumor volume (*upper* panel) and standardized uptake value (SUV; *lower* panel) of the 2-deoxy-2-[^{18}F]fluoro-D-glucose (FDG) tracer were increasing over time, indicating progressive disease. Initiation of treatment led to stabilization of total tumor volume and reduction of lung SUV.

(B) Control scans just prior to treatment highlight extensive tumor metastases in the bone and lung.

(C) Glucose tracer (FDG) uptake in the lung and bone metastases was substantially reduced after 6 months of therapy in imaged sites; further, no new lesions appeared. These data indicate clinical benefit from the drug treatment, manifested as reduced FDG uptake and absence of progression. h = heart, r = renal tubules, b = bladder.

and germline protein-altering variants with gnomAD allele frequency $\leq$ 0.05%). No additional examples of functionally significant variants were found unique to all three 2019 specimens vs. the 2016 specimen (Table S1). Overall, candidates for emergent drug resistance include multiple somatic mutated loci plus significant changes in the CNV landscape.

DISCUSSION

ACC has proven to be a challenging disease, with limited overall response to traditional and targeted therapies. We therefore undertook an experimental approach based on efforts to model its genomic complexity in the context of a personalized approach. Here, we report our results treating a patient with progressive disease that failed to respond to standard-of-care treatments: a novel three-drug cocktail provided stable disease for 12 months, followed by treatment resistance and extensive genomic alterations observed in biopsy samples.

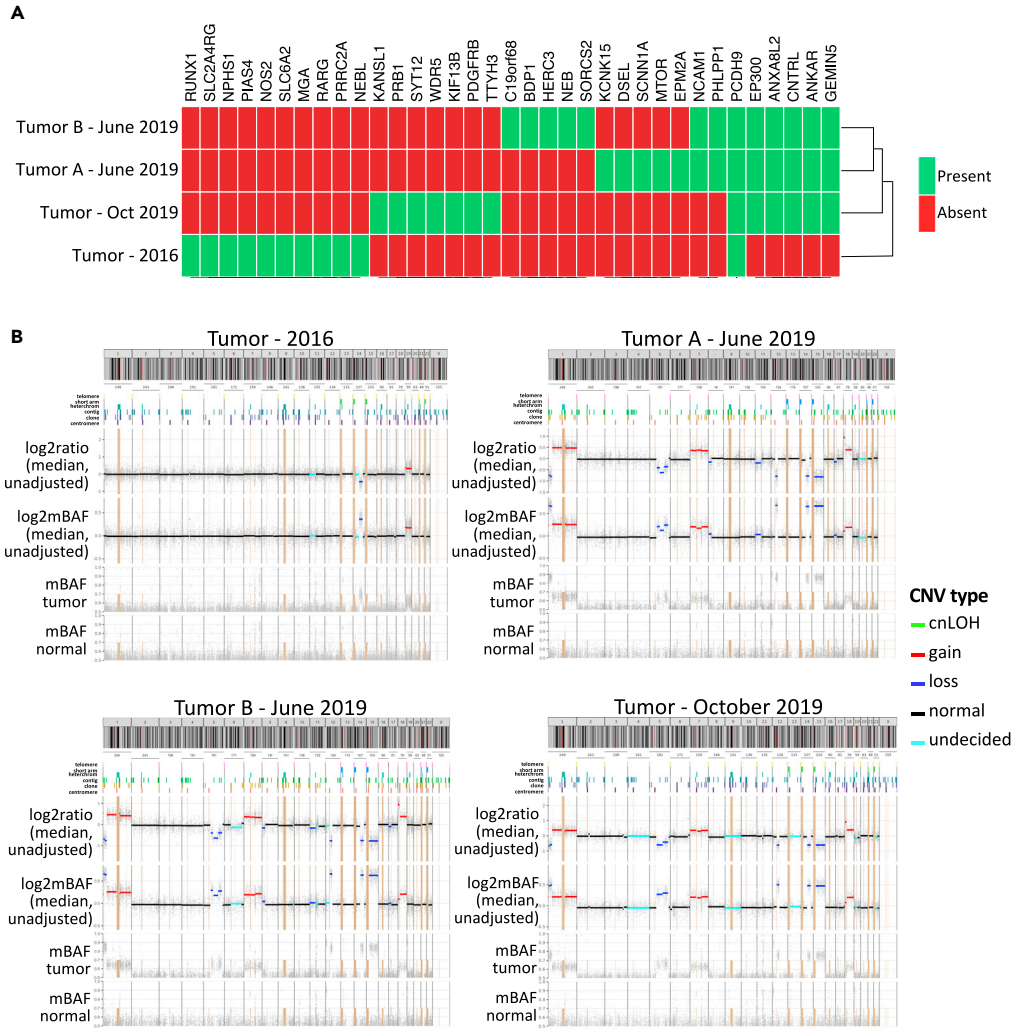

Figure 4. Patient somatic genomic profiles

The patient tumor samples from 2016 to 2019 exhibited significant genomic differences.

(A and B) (A) Somatic protein-altering molecular variants (SNVs and indels with AF ≥ 0.05) and (B) somatic copy number variant (sCNV) profiles of the four tumor samples are summarized, as assessed with saasCNV (Zhang and Hao, 2015). The 2019 specimens contained *de novo* variants and more unstable sCNV profiles.

Building on an approach we previously reported for a patient with advanced colorectal cancer adenocarcinoma (Bangi et al., 2019), we used a decision tree approach to prioritize six genes that were identified as key for affecting tumor progression and, potentially, drug response. Additional tools such immunohistochemistry (Figure 1) were used to help validate our gene choices, but especially given the presence of CNVs and the timeline required for patient treatment, our analysis is necessarily incomplete.

ACC is commonly associated with truncation of MYB and elevated NOTCH1 expression/activity, and this patient's tumor presented with both. ACC tumors are not associated with large numbers of somatic mutations (Ho et al., 2013) and, again, this patient's tumor reflected this as we observed few other somatic changes including CNVs. Germline mutations are often not accounted for in similar analyses. Nevertheless, our germline analysis identified four genes with known functions likely to contribute to tumor progression and potentially drug response: *FAT1* and *FAT3*, *FAT4*, and *ERCC2*, modeled by targeting *kug*, *ft*, and *xpd*, respectively.

FAT1, FAT3, and FAT4 are atypical cadherins and key regulators of cancer-relevant cellular processes including planar cell polarity and MST/HIPPO signaling, which regulates organ size. They are associated

as tumor suppressors in a variety of tumors including ovarian, medullary thyroid, gastric, cervical, colorectal, bladder, and squamous cell carcinomas, as well as ACC (Ho et al., 2013; Gao et al., 2014; Chen et al., 2019; Huang et al., 2019; Skuja et al., 2019; Malgundkar et al., 2020; Melis et al., 2020; Qu et al., 2020; Wang et al., 2020). Reducing these atypical cadherins by approximately 50% expression was therefore considered potentially impactful to our drug screening platform. *ERCC2* encodes XPD, a protein associated with regulation of TFIIH-mediated transcription and DNA damage. XPD has effects on progression of a broad palette of tumor types when mutated or altered—increased or decreased—in expression, and variants in ERCC2 have been associated with altered drug response, especially platinum-based therapies (Du et al., 2014; Fu et al., 2017; Tan et al., 2017; Pajuelo-Lozano et al., 2018; Liu et al., 2019). This may have contributed to the patient's failure to respond to earlier carboplatin-based therapy.

A key advantage of our approach is the ability to identify novel drug combinations selected solely on the basis of efficacy in a whole animal model. The three-drug cocktail—tofacitinib, pindolol, and vorinostat—is especially interesting to consider from a mechanism standpoint. Vorinostat has been reported to provide some benefit to a subset of patients with ACC (Goncalves et al., 2017), though it did not display activity as a single agent in our screens. The primary hit was tofacitinib, a JAK inhibitor used primarily for rheumatoid arthritis. As part of the JAK/STAT pathway, JAK is a signaling kinase with broad effects on development and disease including cancer (Thomas et al., 2015). JAK is positively regulated by NOTCH signaling activity in multiple contexts (Monsalve et al., 2006; Jin et al., 2013; Ho et al., 2015), suggesting a mechanism for tofacitinib activity.

Finally, our genomic analysis of later biopsies highlights the challenge that selection-based resistance poses, even for a three-drug therapeutic cocktail. Our analysis confirmed retention of the MYB-NFIB fusion; however, the CNV landscape was significantly altered including a number of new CNVs in the post-treatment samples. This provides potential insight into the mechanisms by which ACC has proven recalcitrant to most drug treatments: selection for progressive clones can lead to significant genomic changes that can in turn subvert therapeutic activity. One potential response would have been to follow with treatment of our second-line drug cocktail, tofacitinib-gemcitabine. However, follow-up radiation-based therapy and subsequent rapid patient decline made use of gemcitabine contraindicated.

In conclusion, we present a personalized approach to treating ACC. Genomic analysis followed by construction and screening of a "personalized fly avatar" led to a unique three-drug cocktail that promoted stable disease and reduced tumor metabolic activity for 12 months. To date, in our work, this drug cocktail is unique (data not shown), suggesting at least some specificity for this patient. Assessing the broad utility of this whole animal platform approach—and this specific drug cocktail—for patients with ACC will require a larger study. This personalized approach is adaptable to a broad palette of tumor types and may prove especially useful for rare cancers that do not have a standard-of-care second-line therapy or a clear treatment guidance protocol.

Limitations of the study

This study is based on a single patient and, given the divergence between species, should be considered a first step in determining whether this Drosophila approach can provide patient benefits that match or exceed other available approaches.

Resource availability

Lead contact

Further information and requests for resources and reagents should be directed to and will be fulfilled by the lead contact, Ross Cagan (Ross.Cagan@glasgow.ac.uk).

Materials availability

All Drosophila lines generated in this study are available upon request. All data and accession numbers needed to evaluate the conclusions in the paper are present in the paper and/or the supplemental information. Additional data related to this paper may be requested from the authors.

Data and code availability

The published article includes all patient analysis generated during this study except for private genomic data that is restricted due to patient confidentiality.

METHODS

All methods can be found in the accompanying transparent methods supplemental file.

SUPPLEMENTAL INFORMATION

Supplemental information can be found online at https://doi.org/10.1016/j.isci.2021.102212.

ACKNOWLEDGMENTS

We thank the Cagan Laboratory for important discussions and the Genomics Core Facility at the Icahn Institute and Department of Genetics and Genomic Sciences for providing technical support. Computational help and resources were provided by the Department of Scientific Computing at the Icahn School of Medicine at Mount Sinai. A patent application has been filed that is related to this work. This work was supported by funds from the Dean's Office and by NIH-U54OD020353.

AUTHOR CONTRIBUTIONS

Conceptualization: E.B., P.S., K.M., M.P., R.L.C.; Investigation: E.B., P.S., A.U., N.G., A.S.M., A.T., S.G., Y.A., C.H., N.A., C.P., W.Y., D.M., D.L., I.S., C.Y.L., R.S., P.T., M.D.; Formal Analysis including Tumor Board: E.B., J.M., A.U., R.C., A.S.M., H.W., J.G., C.P., M.S., S.K., K.Y., R.S., M.D., K.M., C.A., E.S., M.P., R.L.C.; Writing: E.B., M.P., A.U., H.W., R.L.C.; Project Administration: E.B., I.S., E.S., K.M., M.P., R.L.C.; Funding Acquisition: E.S., R.L.C.

DECLARATION OF INTERESTS

E.B. and R.L.C. are named inventors on patents related to the use of Drosophila to develop cancer treatments including a licensing interest in My Personal Therapeutics. R.L.C. reports being a member of My Personal Therapeutics' advisory board.

Received: November 13, 2020
Revised: January 25, 2021
Accepted: February 17, 2021
Published: March 19, 2021

REFERENCES

Andersson, M.K., and Stenman, G. (2016). The landscape of gene fusions and somatic mutations in salivary gland neoplasms - implications for diagnosis and therapy. Oral Oncol. *57*, 63–69.

Bangi, E., Murgia, C., Teague, A.G., Sansom, O.J., and Cagan, R.L. (2016). Functional exploration of colorectal cancer genomes using Drosophila. Nat. Commun. *7*, 13615.

Bangi, E., Ang, C., Smibert, P., Uzilov, A.V., Teague, A.G., Antipin, Y., Chen, R., Hecht, C., Gruszczynski, N., Yon, W.J., et al. (2019). A personalized platform identifies trametinib plus zoledronate for A patient with KRAS-mutant metastatic colorectal cancer. Sci. Adv. *5*, eaav6528, https://doi.org/10.1126/sciadv.aav6528.

Bischof, J., Maeda, R.K., Hediger, M., Karch, F., and Basler, K. (2007). An optimized transgenesis system for Drosophila using germ-line-specific phiC31 integrases. Proc. Natl. Acad. Sci. U S A *104*, 3312–3317.

Brand, A.H., and Perrimon, N. (1993). Targeted gene expression as a means of altering cell fates and generating dominant phenotypes. Development *118*, 401–415.

Changelian, P.S., Flanagan, M.E., Ball, D.J., Kent, C.R., Magnuson, K.S., Martin, W.H., Rizzuti, B.J., Sawyer, P.S., Perry, B.D., Brissette, W.H., et al. (2003). Prevention of organ allograft rejection by a specific Janus kinase 3 inhibitor. Science *302*, 875–878.

Chen, S., Zhang, N., Shao, J., Wang, T., and Wang, X. (2019). A novel gene signature combination improves the prediction of overall survival in urinary bladder cancer. J. Cancer *10*, 5744–5753.

Coca-Pelaz, A., Rodrigo, J.P., Bradley, P.J., Vander Poorten, V., Triantafyllou, A., Hunt, J.L., Strojan, P., Rinaldo, A., Haigentz, M., Takes, R.P., et al. (2015). Adenoid cystic carcinoma of the head and neck–An update. Oral Oncol. *51*, 652–661.

Creed, S.J., Le, C.P., Hassan, M., Pon, C.K., Albold, S., Chan, K.T., Berginski, M.E., Huang, Z., Bear, J.E., Lane, J.R., et al. (2015). β2-adrenoceptor signaling regulates invadopodia formation to enhance tumor cell invasion. Breast Cancer Res. *17*, 145.

Dar, A.C., Das, T.K., Shokat, K.M., and Cagan, R.L. (2012). Chemical genetic discovery of targets and anti-targets for cancer polypharmacology. Nature *486*, 80–84.

Davidson, C.J., Tirouvanziam, R., Herzenberg, L.A., and Lipsick, J.S. (2005). Functional evolution of the vertebrate Myb gene family: B-Myb, but neither A-Myb nor c-Myb, complements Drosophila Myb in hemocytes. Genetics *169*, 215–229.

Dubendorff, J.W., Whittaker, L.J., Eltman, J.T., and Lipsick, J.S. (1992). Carboxy-terminal elements of c-Myb negatively regulate transcriptional activation in cis and in trans. Genes Dev. *6* (12B), 2524–2535.

Duvic, M., and Vu, J. (2007). Vorinostat: a new oral histone deacetylase inhibitor approved for cutaneous T-cell lymphoma. Expert Opin. Investig. Drugs *16*, 1111–1120, https://doi.org/10.1517/13543784.16.7.1111.

Du, Y., Su, T., Zhao, L., Tan, X., Chang, W., Zhang, H., and Cao, G. (2014). Associations of polymorphisms in DNA repair genes and MDR1 gene with chemotherapy response and survival of non-small cell lung cancer. PLoS one *9*, e99843.

Fitzpatrick, C.A., Sharkov, N.V., Ramsay, G., and Katzen, A.L. (2002). Drosophila myb exerts opposing effects on S phase, promoting proliferation and suppressing endoreduplication. Development *129*, 4497–4507.

Fu, W., Xiao, F., Zhang, R., Li, J., Zhao, D., Lin, X., Xu, Y., Song, X., Xie, Z., Wen, Q., and Yang, X. (2017). Association between the Asp312Asn,

Lys751Gln, and Arg156Arg polymorphisms in XPD and the risk of prostate cancer. Technol. Cancer Res. Treat. *16*, 692–704.

Gao, Y.B., Chen, Z.L., Li, J.G., Hu, X.D., Shi, X.J., Sun, Z.M., Zhang, F., Zhao, Z.R., Li, Z.T., Liu, Z.Y., et al. (2014). Genetic landscape of esophageal squamous cell carcinoma. Nat. Genet. *46*, 1097–1102.

Gatta, G., Guzzo, M., Locati, L.D., McGurk, M., and Prott, F.J. (2020). Major and minor salivary gland tumours. Crit. Rev. Oncol. Hematol. *152*, 102959.

Goncalves, P.H., Heilbrun, L.K., Barrett, M.T., Kummar, S., Hansen, A.R., Siu, L.L., Piekarz, R.L., Sukari, A.W., Chao, J., Pilat, M.J., et al. (2017). A phase 2 study of vorinostat in locally advanced, recurrent, or metastatic adenoid cystic carcinoma. Oncotarget *8*, 32918–32929.

Gonda, T.J., Buckmaster, C., and Ramsay, R.G. (1989). Activation of c-myb by carboxy-terminal truncation: relationship to transformation of murine haemopoietic cells in vitro. EMBO J. *8*, 1777–1783.

Ho, A.S., Kannan, K., Roy, D.M., Morris, L.G., Ganly, I., Katabi, N., Ramaswami, D., Walsh, L.A., Eng, S., Huse, J.T., et al. (2013). The mutational landscape of adenoid cystic carcinoma. Nat. Genet. *45*, 791–798.

Ho, A.S., Ochoa, A., Jayakumaran, G., Zehir, A., Valero Mayor, C., Tepe, J., Makarov, V., Dalin, M.G., He, J., Bailey, M., et al. (2019). Genetic hallmarks of recurrent/metastatic adenoid cystic carcinoma. J. Clin. Invest. *129*, 4276–4289.

Ho, D.M., Pallavi, S.K., and Artavanis-Tsakonas, S. (2015). The Notch-mediated hyperplasia circuitry in Drosophila reveals a Src-JNK signaling axis. eLife *4*, e05996.

Huang, J., Qian, Z., Gong, Y., Wang, Y., Guan, Y., Han, Y., Yi, X., Huang, W., Ji, L., Xu, J., et al. (2019). Comprehensive genomic variation profiling of cervical intraepithelial neoplasia and cervical cancer identifies potential targets for cervical cancer early warning. J. Med. Genet. *56*, 186–194.

Jin, S., Mutvei, A.P., Chivukula, I.V., Andersson, E.R., Ramsköld, D., Sandberg, R., Lee, K.L., Kronqvist, P., Mamaeva, V., Ostling, P., et al. (2013). Non-canonical Notch signaling activates IL-6/JAK/STAT signaling in breast tumor cells and is controlled by p53 and IKKα/IKKβ. Oncogene *32*, 4892–4902.

Kircher, M., Witten, D.M., Jain, P., O'Roak, B.J., Cooper, G.M., and Shendure, J. (2014). A general framework for estimating the relative pathogenicity of human genetic variants. Nat. Genet. *46*, 310–315.

Levine, B.D., and Cagan, R.L. (2016). Drosophila lung cancer models identify trametinib plus statin as candidate therapeutic. Cell Rep. *14*, 1477–1487.

Levinson, S., and Cagan, R.L. (2016). Drosophila cancer models identify functional differences between ret fusions. Cell Rep. *16*, 3052–3061.

Lipsick, J.S., Manak, J., Mitiku, N., Chen, C.K., Fogarty, P., and Guthrie, E. (2001). Functional evolution of the Myb oncogene family. Blood Cells Mol. Dis. *27*, 456–458.

Liu, X., Wu, C., Li, C., and Boerwinkle, E. (2016). dbNSFP v3.0: a one-stop Database of functional predictions and annotations for human nonsynonymous and splice-site SNVs. Hum. Mutat. *37*, 235–241.

Liu, Z., Kong, J., Kong, Y., Cai, F., Xu, X., Liu, J., and Wang, S. (2019). Association of XPD Asp312Asn polymorphism and response to oxaliplatin-based first-line chemotherapy and survival in patients with metastatic colorectal cancer. Adv. Clin. Exp. Med. *28*, 1459–1468.

Malgundkar, S.H., Burney, I., Al Moundhri, M., Al Kalbani, M., Lakhtakia, R., Okamoto, A., and Tamimi, Y. (2020). FAT4 silencing promotes epithelial-to-mesenchymal transition and invasion via regulation of YAP and β-catenin activity in ovarian cancer. BMC Cancer *20*, 374.

Marks, P.A., and Breslow, R. (2007). Dimethyl sulfoxide to vorinostat: development of this histone deacetylase inhibitor as an anticancer drug. Nat. Biotechnol. *25*, 84–90.

Matsuno, K., Ito, M., Hori, K., Miyashita, F., Suzuki, S., Kishi, N., Artavanis-Tsakonas, S., and Okano, H. (2002). Involvement of a proline-rich motif and RING-H2 finger of Deltex in the regulation of Notch signaling. Development *129*, 1049–1059.

Melis, M., Zhang, T., Scognamiglio, T., and Gudas, L.J. (2020). Mutations in long-lived epithelial stem cells and their clonal progeny in pre-malignant lesions and in oral squamous cell carcinoma. Carcinogenesis *41*, 1553, https://doi.org/10.1093/carcin/bgaa019.

Mitani, Y., Liu, B., Rao, P.H., Borra, V.J., Zafereo, M., Weber, R.S., Kies, M., Lozano, G., Futreal, P.A., Caulin, C., and El-Naggar, A.K. (2016). Novel MYBL1 gene rearrangements with recurrent MYBL1-NFIB fusions in salivary adenoid cystic carcinomas lacking t(6;9) translocations. Clin. Cancer Res. *22*, 725–733.

Monsalve, E., Pérez, M.A., Rubio, A., Ruiz-Hidalgo, M.J., Baladrón, V., García-Ramírez, J.J., Gómez, J.C., Laborda, J., and Díaz-Guerra, M.J. (2006). Notch-1 up-regulation and signaling following macrophage activation modulates gene expression patterns known to affect antigen-presenting capacity and cytotoxic activity. J. Immunol. *176*, 5362–5373.

Na, Z., Qiao, X., Hao, X., Fan, L., Xiao, Y., Shao, Y., Sun, M., Feng, Z., Guo, W., Li, J., et al. (2018). The effects of beta-blocker use on cancer prognosis: a meta-analysis based on 319,006 patients. Onco Targets Ther. *11*, 4913–4944.

Ni, J.Q., Zhou, R., Czech, B., Liu, L.P., Holderbaum, L., Yang-Zhou, D., Shim, H.S., Tao, R., Handler, D., Karpowicz, P., et al. (2011). A genome-scale shRNA resource for transgenic RNAi in Drosophila. Nat. Methods *8*, 405–407.

Ouyang, D.Q., Liang, L.Z., Zheng, G.S., Ke, Z.F., Weng, D.S., Yang, W.F., Su, Y.X., and Liao, G.Q. (2017). Risk factors and prognosis for salivary gland adenoid cystic carcinoma in southern China: a 25-year retrospective study. Medicine (Baltimore) *96*, e5964.

Pajuelo-Lozano, N., Bargiela-Iparraguirre, J., Dominguez, G., Quiroga, A.G., Perona, R., and Sanchez-Perez, I. (2018). XPA, XPC, and XPD modulate sensitivity in gastric cisplatin resistance cancer cells. Front. Pharmacol. *9*, 1197.

Partecke, L.I., Speerforck, S., Käding, A., Seubert, F., Kühn, S., Lorenz, E., Schwandke, S., Sendler, M., Keßler, W., Trung, D.N., et al. (2016). Chronic stress increases experimental pancreatic cancer growth, reduces survival and can be antagonised by beta-adrenergic receptor blockade. Pancreatology *16*, 423–433.

Persson, M., Andrén, Y., Mark, J., Horlings, H.M., Persson, F., and Stenman, G. (2009). Recurrent fusion of MYB and NFIB transcription factor genes in carcinomas of the breast and head and neck. Proc. Natl. Acad. Sci. U S A *106*, 18740–18744.

Persson, M., Andrén, Y., Moskaluk, C.A., Frierson, H.F., Cooke, S.L., Futreal, P.A., Kling, T., Nelander, S., Nordkvist, A., Persson, F., and Stenman, G. (2012). Clinically significant copy number alterations and complex rearrangements of MYB and NFIB in head and neck adenoid cystic carcinoma. Genes Chromosomes Cancer *51*, 805–817.

Plunkett, W., Huang, P., Xu, Y.Z., Heinemann, V., Grunewald, R., and Gandhi, V. (1995). Gemcitabine: metabolism, mechanisms of action, and self-potentiation. Semin. Oncol. *22*, 3–10.

Qu, N., Shi, X., Zhao, J.-J., Guan, H., Zhang, T.-T., Wen, S.-S., Liao, T., Hu, J.-Q., Liu, W.-Y., Wang, Y.-L., et al. (2020). Genomic and transcriptomic characterization of sporadic medullary thyroid carcinoma. Thyroid *30*, 1025–1036.

Rettig, E.M., Talbot, C.C., Sausen, M., Jones, S., Bishop, J.A., Wood, L.D., Tokheim, C., Niknafs, N., Karchin, R., Fertig, E.J., et al. (2016). Whole-genome sequencing of salivary gland adenoid cystic carcinoma. Cancer Prev. Res. (Phila) *9*, 265–274.

Ross, J.S., Wang, K., Rand, J.V., Sheehan, C.E., Jennings, T.A., Al-Rohil, R.N., Otto, G.A., Curran, J.C., Palmer, G., Downing, S.R., et al. (2014). Comprehensive genomic profiling of relapsed and metastatic adenoid cystic carcinomas by next-generation sequencing reveals potential new routes to targeted therapies. Am. J. Surg. Pathol. *38*, 235–238.

Rudrapatna, V.A., Bangi, E., and Cagan, R.L. (2014). A Jnk-Rho-Actin remodeling positive feedback network directs Src-driven invasion. Oncogene *33*, 2801–2806.

Sakura, H., Kanei-Ishii, C., Nagase, T., Nakagoshi, H., Gonda, T.J., and Ishii, S. (1989). Delineation of three functional domains of the transcriptional activator encoded by the c-myb protooncogene. Proc. Natl. Acad. Sci. U S A *86*, 5758–5762.

Skuja, E., Butane, D., Nakazawa-Miklasevica, M., Daneberga, Z., Purkalne, G., and Miklasevics, E. (2019). Deletions in metastatic colorectal cancer with chromothripsis. Exp. Oncol. *41*, 323–327.

Sondka, Z., Bamford, S., Cole, C.G., Ward, S.A., Dunham, I., and Forbes, S.A. (2018). The COSMIC Cancer Gene Census: describing genetic dysfunction across all human cancers. Nat. Rev. Cancer *18*, 696–705.

Sonoshita, M., Scopton, A.P., Ung, P.M.U., Murray, M.A., Silber, L., Maldonado, A.Y., Real, A., Schlessinger, A., Cagan, R.L., and Dar, A.C. (2018). A whole-animal platform to advance a clinical kinase inhibitor into new disease space. Nat. Chem. Biol. *14*, 291–298.

Stephens, P.J., Davies, H.R., Mitani, Y., Van Loo, P., Shlien, A., Tarpey, P.S., Papaemmanuil, E., Cheverton, A., Bignell, G.R., Butler, A.P., et al. (2013). Whole exome sequencing of adenoid cystic carcinoma. J. Clin. Invest. *123*, 2965–2968.

Tan, L.M., Qiu, C.F., Zhu, T., Jin, Y.X., Li, X., Yin, J.Y., Zhang, W., Zhou, H.H., and Liu, Z.Q. (2017). Genetic polymorphisms and platinum-based chemotherapy treatment outcomes in patients with non-small cell lung cancer: a genetic Epidemiology study based meta-analysis. Sci. Rep. *7*, 5593.

Tchekmedyian, V., Sherman, E.J., Dunn, L., Tran, C., Baxi, S., Katabi, N., Antonescu, C.R., Ostrovnaya, I., Haque, S.S., Pfister, D.G., and Ho, A.L. (2019). Phase II study of lenvatinib in patients with progressive, recurrent or metastatic adenoid cystic carcinoma. J. Clin. Oncol. *37*, 1529–1537, https://doi.org/10.1200/jco.18.01859.

Thomas, S.J., Snowden, J.A., Zeidler, M.P., and Danson, S.J. (2015). The role of JAK/STAT signalling in the pathogenesis, prognosis and treatment of solid tumours. Br. J. Cancer *113*, 365–371.

Vert, J.P., Foveau, N., Lajaunie, C., and Vandenbrouck, Y. (2006). An accurate and interpretable model for siRNA efficacy prediction. BMC Bioinformatics *7*, 520.

Vidal, M., Warner, S., Read, R., and Cagan, R.L. (2007). Differing Src signaling levels have distinct outcomes in Drosophila. Cancer Res. *67*, 10278–10285.

Vidal, M., Larson, D.E., and Cagan, R.L. (2006). Csk-deficient boundary cells are eliminated from normal Drosophila epithelia by exclusion, migration, and apoptosis. Dev. Cell *10*, 33–44.

Vyas, D., O'Dell, K.M., Bandy, J.L., and Boyce, E.G. (2013). Tofacitinib: the First Janus Kinase (JAK) inhibitor for the treatment of rheumatoid arthritis. Ann. Pharmacother. *47*, 1524–1531.

Wang, H., Shen, L., Li, Y., and Lv, J. (2020). Integrated characterisation of cancer genes identifies key molecular biomarkers in stomach adenocarcinoma. J. Clin. Pathol. *73*, 579–586.

Weston, K., and Bishop, J.M. (1989). Transcriptional activation by the v-myb oncogene and its cellular progenitor, c-myb. Cell *58*, 85–93.

West, R.B., Kong, C., Clarke, N., Gilks, T., Lipsick, J.S., Cao, H., Kwok, S., Montgomery, K.D., Varma, S., and Le, Q.T. (2011). MYB expression and translocation in adenoid cystic carcinomas and other salivary gland tumors with clinicopathologic correlation. Am. J. Surg. Pathol. *35*, 92–99.

Wrobel, L.J., Bod, L., Lengagne, R., Kato, M., Prévost-Blondel, A., and Gal, F.-A.L. (2016). Propranolol induces a favourable shift of anti-tumor immunity in a murine spontaneous model of melanoma. Oncotarget *7*, 77825–77837, https://doi.org/10.18632/oncotarget.12833.

Zhang, Z., and Hao, K. (2015). SAAS-CNV: a Joint segmentation approach on Aggregated and allele specific signals for the identification of somatic copy number alterations with next-generation sequencing data. PLoS Comput. Biol. *11*, e1004618.

iScience, Volume *24*

Supplemental information

A Drosophila platform identifies a novel, personalized therapy for a patient with adenoid cystic carcinoma

Erdem Bangi, Peter Smibert, Andrew V. Uzilov, Alexander G. Teague, Sindhura Gopinath, Yevgeniy Antipin, Rong Chen, Chana Hecht, Nelson Gruszczynski, Wesley J. Yon, Denis Malyshev, Denise Laspina, Isaiah Selkridge, Huan Wang, Jorge Gomez, John Mascarenhas, Aye S. Moe, Chun Yee Lau, Patricia Taik, Chetanya Pandya, Max Sung, Sara Kim, Kendra Yum, Robert Sebra, Michael Donovan, Krzysztof Misiukiewicz, Celina Ang, Eric E. Schadt, Marshall R. Posner, and Ross L. Cagan

Supplemental Data

Figure S1

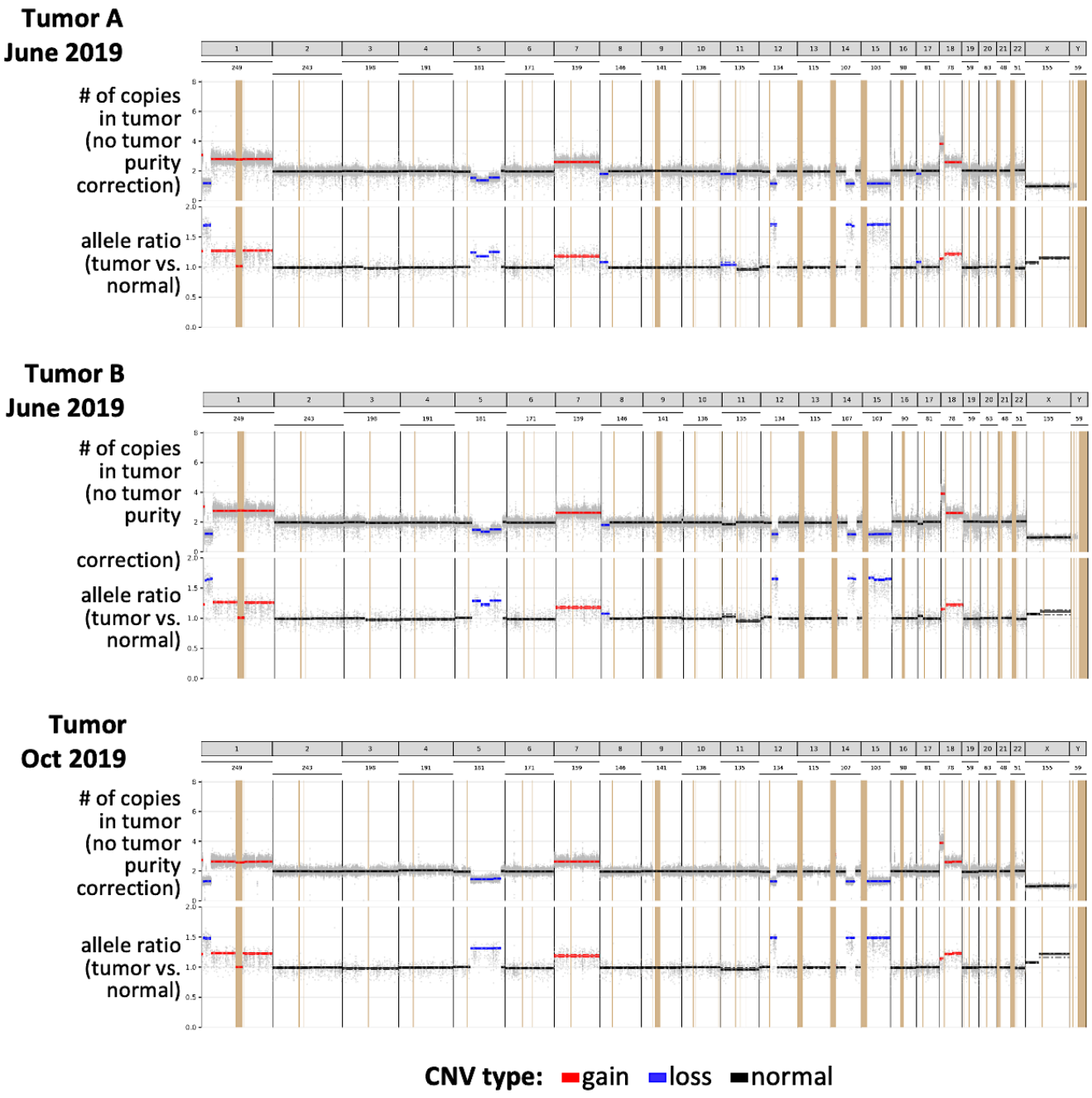

Figure S1: 2019 samples- sCNV profiles; related to Figure 4: GATK4 Somatic CNV algorithm-based profiles of the 2019 specimens are consistent with results from the saasCNV analysis shown in Figure 4.

Table S1

specimen	chrom	pos	ref	alt	AD	Ref_AD	AF	gene_symbol	hgvs_p	effect_seqontology
tumor-2016	6	31600001	G	C	59	172	0.2554	PRRC2A	p.Gly1184Ala	missense_variant
tumor-2016	10	21178863	C	T	49	126	0.28	NEBL	p.Glu57Lys	missense_variant
tumor-2016	12	53605638	C	T	25	67	0.2717	RARG	p.Arg396Lys	missense_variant
tumor-2016	13	67800268	G	A	119	320	0.2711	PCDH9	p.Leu769Phe	missense_variant
tumor-2016	15	42005433	GTA	G	95	253	0.273	MGA	p.Val1057fs	frameshift_variant
tumor-2016	16	55703560	A	G	43	124	0.2575	SLC6A2	p.Asn120Asp	missense_variant
tumor-2016	17	26092584	C	T	8	71	0.1013	NOS2	p.Arg802His	missense_variant
tumor-2016	19	4012931	TGAGTTTTC	T	150	526	0.2219	PIAS4	p.Met13fs	frameshift_variant
tumor-2016	19	36339588	C	T	24	143	0.1437	NPHS1	p.Trp374*	stop_gained
tumor-2016	20	62373487	C	CG	46	144	0.2421	SLC2A4RG	p.Pro195_Ala196fs	frameshift_variant
tumor-2016	21	36231810	C	T	79	227	0.2582	RUNX1	p.Ala165Thr	missense_variant
tumor-A-Jun-2019	1	11227539	G	A	4	65	0.058	MTOR	p.Ala1430Val	missense_variant
tumor-A-Jun-2019	2	190575865	G	T	44	136	0.2444	ANKAR	p.Cys737Phe	missense_variant
tumor-A-Jun-2019	5	154300980	G	A	42	108	0.28	GEMIN5	p.Pro462Leu	missense_variant
tumor-A-Jun-2019	6	146056511	G	GCA	2	12	0.1429	EPM2A	p.Arg41_Pro42fs	frameshift_variant
tumor-A-Jun-2019	9	123902923	A	G	36	68	0.3462	CNTRL	p.Asp781Gly	missense_variant
tumor-A-Jun-2019	9	123902923	A	G	36	68	0.3462	CNTRL	p.Asp229Gly	missense_variant
tumor-A-Jun-2019	10	47756088	C	G	45	131	0.2557	ANXA8L2	p.Ala183Gly	missense_variant
tumor-A-Jun-2019	11	113103461	G	T	32	245	0.1155	NCAM1	p.Asp473Tyr	missense_variant
tumor-A-Jun-2019	12	6458572	CTGT	CACA	8	124	0.0606	SCNN1A	NULL	splice_acceptor_variant
tumor-A-Jun-2019	13	67800268	G	A	129	134	0.4905	PCDH9	p.Leu769Phe	missense_variant
tumor-A-Jun-2019	18	60382986	CCGGCGGCCGCC GCTGCGGCAGCA GCAGCAGCAG CGGCGGCCG	C	3	20	0.1304	PHLPP1	p.Pro24_Ala38del	inframe_deletion
tumor-A-Jun-2019	18	65179718	T	A	26	336	0.0718	DSEL	p.Asn720Tyr	missense_variant
tumor-A-Jun-2019	20	43379283	C	G	5	78	0.0602	KCNK15	p.Pro266Arg	missense_variant
tumor-A-Jun-2019	22	41489055	C	CT	25	185	0.119	EP300	p.Pro16_Lys17fs	frameshift_variant
tumor-B-Jun-2019	2	152521368	TGTA	T	9	121	0.0692	NEB	p.Tyr1749del	inframe_deletion
tumor-B-Jun-2019	2	190575865	G	T	35	141	0.1989	ANKAR	p.Cys737Phe	missense_variant
tumor-B-Jun-2019	4	7194621	A	G	2	6	0.25	SORCS2	p.Asp83Gly	missense_variant
tumor-B-Jun-2019	4	89570991	A	AG	5	91	0.0521	HERC3	p.Glu76_Gln77fs	frameshift_variant
tumor-B-Jun-2019	5	70828195	CCAAA	C	7	88	0.0737	BDP1	p.Pro1945fs	frameshift_variant
tumor-B-Jun-2019	5	154300980	G	A	18	80	0.1837	GEMIN5	p.Pro462Leu	missense_variant
tumor-B-Jun-2019	9	123902923	A	G	39	61	0.39	CNTRL	p.Asp781Gly	missense_variant
tumor-B-Jun-2019	9	123902923	A	G	39	61	0.39	CNTRL	p.Asp229Gly	missense_variant
tumor-B-Jun-2019	10	47756088	C	G	40	101	0.2837	ANXA8L2	p.Ala183Gly	missense_variant
tumor-B-Jun-2019	11	113103461	G	T	14	228	0.0579	NCAM1	p.Asp473Tyr	missense_variant
tumor-B-Jun-2019	13	67800268	G	A	82	152	0.3504	PCDH9	p.Leu769Phe	missense_variant
tumor-B-Jun-2019	18	60382986	CCGGCGGCCGCCGC TGCGGCAGCAGCAG CAGCAGCGGCGGCCG	C	3	18	0.1429	PHLPP1	p.Pro24_Ala38del	inframe_deletion
tumor-B-Jun-2019	19	48698259	GCGT	G	3	28	0.0968	C19orf68	p.Arg313_Val314del	disruptive_inframe_del..
tumor-B-Jun-2019	22	41489055	C	CT	22	165	0.1176	EP300	p.Pro16_Lys17fs	frameshift_variant
tumor-Oct-2019	2	190575865	G	T	82	256	0.2426	ANKAR	p.Cys737Phe	missense_variant
tumor-Oct-2019	5	149505023	C	A	18	287	0.059	PDGFRB	p.Asp598Tyr	missense_variant
tumor-Oct-2019	5	154300980	G	A	27	228	0.1059	GEMIN5	p.Pro462Leu	missense_variant
tumor-Oct-2019	7	2701363	G	GCAGCC	49	504	0.0886	TTYH3	p.Gly521_Ser522fs	frameshift_variant
tumor-Oct-2019	8	28980986	G	A	67	328	0.1696	KIF13B	p.Arg1126Cys	missense_variant
tumor-Oct-2019	9	123902923	A	G	74	142	0.3426	CNTRL	p.Asp781Gly	missense_variant
tumor-Oct-2019	9	123902923	A	G	74	142	0.3426	CNTRL	p.Asp229Gly	missense_variant
tumor-Oct-2019	9	137020477	G	C	43	360	0.1067	WDR5	p.Trp241Cys	missense_variant
tumor-Oct-2019	10	47756088	C	G	95	287	0.2487	ANXA8L2	p.Ala183Gly	missense_variant
tumor-Oct-2019	11	66816217	C	T	34	314	0.0977	SYT12	p.Arg419Trp	missense_variant
tumor-Oct-2019	12	11506922	G	C	216	446	0.3263	PRB1	p.Pro39Ala	missense_variant
tumor-Oct-2019	13	67800268	G	A	169	344	0.3294	PCDH9	p.Leu769Phe	missense_variant
tumor-Oct-2019	17	44110767	A	ACCTCT TCATTCTC CTCATCAGGACTCC CCTTCAGAGACTG	146	228	0.3904	KANSL1	NULL	splice_donor_variant
tumor-Oct-2019	22	41489055	C	CT	29	355	0.0755	EP300	p.Pro16_Lys17fs	frameshift_variant

Table S1: List of variants identified for the four patient tumor samples; related to Figure 1: Note conserved alterations in ANKAR, ANXA8L2, CNTRL, EP300, and GEMIN5 in the 2019 samples. Only the variant in PCDH9 was common to all samples; this was not included in the avatar models because it was not predicted to alter protein function.

Table S2

sample	Call Type	Num Genes	Seg Chrom	segL	segR	Seg Len	Segment Cytoband	Tumor Num Copies	Tumor Num Copies_ciLow	Tumor Num Copies_ciHigh
tumor-Oct-2019	loss	395	chr12	39047434	62261456	23214023	q12q14.1	1.3088	1.3027	1.3143
tumor-Oct-2019	gain	578	chr1	152329836	196716693	44386858	q21.3q31.3	2.6268	2.6182	2.6314
tumor-Oct-2019	loss	270	chr14	54863537	86090091	31226555	q22.2q31.3	1.3071	1.3013	1.3111
tumor-Oct-2019	gain	573	chr1	196857031	249212550	52355520	q31.3q44	2.6372	2.6328	2.6437
tumor-Oct-2019	loss	393	chr1	13182741	34401805	21219065	p36.21p35.1	1.3214	1.3169	1.3257
tumor-Oct-2019	gain	1412	chr7	192950	158937713	158744764	p22.3q36.3	2.6379	2.6327	2.6443
tumor-Oct-2019	gain	126	chr18	18531095	44497558	25966464	q11.1q21.1	2.6021	2.5939	2.6131
tumor-Oct-2019	loss	1013	chr15	20739247	102359139	81619893	q11.2q26.3	1.3155	1.3111	1.3198
tumor-Oct-2019	gain	840	chr1	34497945	120548461	86050517	p35.1p12	2.6399	2.6347	2.6449
tumor-Oct-2019	loss	215	chr5	140865491	167182447	26316957	q31.3q34	1.4964	1.4917	1.501
tumor-Oct-2019	gain	116	chr18	158449	14852729	14694281	p11.32p11.21	3.8927	3.8809	3.9044
tumor-Oct-2019	gain	180	chr1	145414532	152329835	6915304	q21.1q21.3	2.5896	2.5764	2.5998
tumor-Oct-2019	loss	614	chr5	60394569	140865490	80470922	q12.1q31.3	1.4549	1.4524	1.4595
tumor-Oct-2019	gain	185	chr18	44559124	78005481	33446358	q21.1q23	2.6297	2.6192	2.6418
tumor-Oct-2019	loss	125	chr1	5987459	12908010	6920552	p36.31p36.21	1.3051	1.2988	1.3114
tumor-Oct-2019	gain	106	chr1	861072	5969523	5108452	p36.33p36.31	2.7424	2.7338	2.7503
tumor-Oct-2019	gain	42	chr1	120611698	145368934	24757237	p11.2q21.1	2.5783	2.5486	2.6098
tumor-Oct-2019	gain	16	chr14	19377344	20296357	919014	q11.2	3.1031	3.0291	3.2005
tumor-Oct-2019	loss	2	chr1	196743767	196801379	57613	q31.3	1.1489	1.1152	1.183
tumor-Oct-2019	gain	8	chr12	11174021	11286633	112613	p13.2	2.0581	1.9823	2.1423
tumor-Oct-2019	loss	10	chr1	12908011	13001563	93553	p36.21	0.0565	0.0507	0.0639
tumor-Oct-2019	loss	4	chr18	44554323	44555322	1000	q21.1	0.0014	0.0012	0.0015
tumor-Oct-2019	loss	2	chrX	47917607	47920574	2968	p11.23	0.0064	0.0059	0.0068
tumor-Oct-2019	loss	1	chr2	131413872	131415700	1829	q21.1	0.0115	0.0105	0.0125
tumor-A-Jun-2019	loss	395	chr12	39047434	62261456	23214023	q12q14.1	1.1526	1.1475	1.1561
tumor-A-Jun-2019	gain	1331	chr1	145414532	249212550	103798019	q21.1q44	2.8002	2.7877	2.8078
tumor-A-Jun-2019	loss	179	chr14	54863537	74194477	19330941	q22.2q24.3	1.1513	1.1466	1.1581
tumor-A-Jun-2019	loss	393	chr1	13182741	34401805	21219065	p36.21p35.1	1.1775	1.1715	1.1859
tumor-A-Jun-2019	gain	1412	chr7	192950	158937713	158744764	p22.3q36.3	2.6028	2.5908	2.6117
tumor-A-Jun-2019	gain	314	chr18	18531095	78005481	59474387	q11.1q23	2.5895	2.5789	2.5976
tumor-A-Jun-2019	loss	669	chr15	42985064	102359139	59374076	q15.2q26.3	1.1594	1.1546	1.1697
tumor-A-Jun-2019	gain	848	chr1	34497945	121116297	86618353	p35.1p11.2	2.8008	2.7886	2.8145
tumor-A-Jun-2019	loss	441	chr5	123974576	162945619	38971044	q23.2q34	1.5554	1.5481	1.5595
tumor-A-Jun-2019	loss	345	chr15	20739247	42977063	22237817	q11.2q15.2	1.1552	1.1515	1.1621
tumor-A-Jun-2019	gain	116	chr18	158449	14852729	14694281	p11.32p11.21	3.8233	3.807	3.8418
tumor-A-Jun-2019	loss	88	chr14	74326992	86090091	11763100	q24.3q31.3	1.1545	1.1483	1.1587
tumor-A-Jun-2019	loss	205	chr5	79733325	123973849	44240525	q14.1q23.2	1.3682	1.3618	1.377
tumor-A-Jun-2019	loss	122	chr1	5987459	12888773	6901315	p36.31p36.21	1.1786	1.1727	1.1859
tumor-A-Jun-2019	loss	160	chr5	60240509	79733324	19492816	q12.1q14.1	1.5339	1.5258	1.5405
tumor-A-Jun-2019	gain	106	chr1	861072	5969523	5108452	p36.33p36.31	3.0759	3.0619	3.0942
tumor-A-Jun-2019	gain	37	chr1	121116437	145368934	24252498	p11.2q21.1	2.7728	2.7478	2.8062
tumor-A-Jun-2019	gain	16	chr14	19377344	20296357	919014	q11.2	2.3845	2.3168	2.469
tumor-A-Jun-2019	gain	8	chr12	11174021	11286633	112613	p13.2	2.0068	1.9197	2.1123
tumor-A-Jun-2019	loss	1	chr15	42977064	42985063	8000	q15.2	1.1922	1.1484	1.2691
tumor-A-Jun-2019	loss	1	chr14	74196093	74206961	10869	q24.3	1.1567	1.101	1.2223
tumor-A-Jun-2019	loss	10	chr1	12907011	13001563	94553	p36.21	0.0433	0.0399	0.0451
tumor-A-Jun-2019	loss	2	chrX	47917607	47920574	2968	p11.23	0	0	0
tumor-A-Jun-2019	loss	295	chr8	190646	30242924	30052279	p23.3p12	1.8007	1.7915	1.8084
tumor-A-Jun-2019	loss	401	chr17	5757	18287151	18281395	p13.3p11.2	1.8082	1.8023	1.8157
tumor-A-Jun-2019	loss	634	chr11	192850	56128923	55936074	p15.5q12.1	1.7992	1.7873	1.8075
tumor-A-Jun-2019	loss	2	chr3	75785779	75787778	2000	p12.3	0.0096	0.0083	0.0105
tumor-A-Jun-2019	loss	6	chr17	18291283	18395935	104653	p11.2	1.3259	1.2337	1.4274
tumor-B-Jun-2019	loss	395	chr12	39047434	62261456	23214023	q12q14.1	1.1898	1.1869	1.1947
tumor-B-Jun-2019	gain	1331	chr1	145414532	249212550	103798019	q21.1q44	2.7593	2.7489	2.7681
tumor-B-Jun-2019	loss	179	chr14	54866362	74194477	19328116	q22.2q24.3	1.1794	1.1731	1.1846
tumor-B-Jun-2019	loss	188	chr1	24424163	34401805	9977643	p36.11p35.1	1.211	1.2062	1.2178
tumor-B-Jun-2019	gain	1412	chr7	192950	158937713	158744764	p22.3q36.3	2.6255	2.6116	2.6337
tumor-B-Jun-2019	gain	314	chr18	18531095	78005481	59474387	q11.1q23	2.6095	2.5998	2.6272
tumor-B-Jun-2019	loss	244	chr15	79069536	102359139	23289604	q25.1q26.3	1.2001	1.1934	1.2064
tumor-B-Jun-2019	gain	848	chr1	34497945	121116297	86618353	p35.1p11.2	2.7527	2.7364	2.7689
tumor-B-Jun-2019	loss	445	chr5	122491328	162945619	40454292	q23.2q34	1.5062	1.5006	1.512
tumor-B-Jun-2019	loss	293	chr15	20739247	40913587	20174341	q11.2q15.1	1.1763	1.1689	1.1841
tumor-B-Jun-2019	gain	116	chr18	158449	14852729	14694281	p11.32p11.21	3.9075	3.8853	3.9292
tumor-B-Jun-2019	loss	206	chr1	13182741	24411379	11228639	p36.21p36.11	1.2163	1.2129	1.2203
tumor-B-Jun-2019	loss	88	chr14	74326992	86090091	11763100	q24.3q31.3	1.1811	1.1744	1.1864
tumor-B-Jun-2019	loss	478	chr15	40917588	79063786	38146199	q15.1q25.1	1.1926	1.1833	1.1971
tumor-B-Jun-2019	loss	213	chr5	60394569	89990456	29595888	q12.1q14.3	1.4784	1.4702	1.4894
tumor-B-Jun-2019	loss	122	chr1	5987459	12888773	6901315	p36.31p36.21	1.2146	1.2079	1.2195
tumor-B-Jun-2019	gain	106	chr1	861072	5969523	5108452	p36.33p36.31	3.0404	3.0221	3.0619

tumor-B-Jun-2019	gain	37	chr1	121116437	145368934	24252498	p11.2q21.1	2.77	2.7297	2.798
tumor-B-Jun-2019	loss	147	chr5	89992504	122435906	32443403	q14.3q23.2	1.3518	1.3437	1.3563
tumor-B-Jun-2019	gain	16	chr14	19377344	20296357	919014	q11.2	2.3562	2.2822	2.4738
tumor-B-Jun-2019	gain	8	chr12	11174021	11286633	112613	p13.2	1.9849	1.8989	2.0369
tumor-B-Jun-2019	loss	1	chr14	74196093	74206961	10869	q24.3	1.1603	0	1.2757
tumor-B-Jun-2019	loss	1	chr15	79063787	79069433	5647	q25.1	1.1365	1.0675	1.1912
tumor-B-Jun-2019	loss	1	chr15	40913588	40917587	4000	q15.1	1.1748	1.1129	1.2248
tumor-B-Jun-2019	loss	10	chr1	12907011	13001563	94553	p36.21	0.1924	0.1692	0.687
tumor-B-Jun-2019	loss	1	chr1	24412884	24422226	9343	p36.11	1.1673	1.122	1.2056
tumor-B-Jun-2019	loss	2	chrX	47917607	47920574	2968	p11.23	0.0012	0.0011	0.0014
tumor-B-Jun-2019	loss	3	chr2	131413872	131487474	73603	q21.1	1.6924	1.5345	1.9158
tumor-B-Jun-2019	loss	295	chr8	190646	30242924	30052279	p23.3p12	1.8051	1.7991	1.8129
tumor-B-Jun-2019	loss	2	chr3	75785779	75787778	2000	p12.3	0.0116	0.0101	0.0133

Table S2: GATK4 somatic gene variant analysis; related to Figure 1: sCNV segmentation profiles of 2019 specimens as determined by the GATK4 somatic CNV algorithm.

Table S3

chrom	pos	ref	alt	gene symbol	transcript	protein change
chr1	6947717	C	T	CAMTA1	NM_001242701.1	p.Leu80Phe
chr1	14106394	A	ACTC	PRDM2	NM_012231.4	p.Pro703dup
chr1	14143003	A	G	PRDM2	NM_001135610.1	p.Gln198Arg
chr1	15832543	T	C	CASP9	NM_001229.4	p.Gln221Arg
chr1	15850613	G	A	CASP9	NM_001229.4	p.Ala28Val
chr1	17991052	T	C	ARHGEF10L	NM_018125.3	p.Trp991Arg
chr1	18023690	A	G	ARHGEF10L	NM_018125.3	p.Ile1219Val
chr1	23885498	T	C	ID3	NM_002167.4	p.Thr105Ala
chr5	68695940	T	G	RAD17	NM_133339.2	p.Leu557Arg
chr5	112176756	T	A	APC	NM_000038.5	p.Val1822Asp
chr12	49447416	G	C	KMT2D	NM_003482.3	p.Arg228Gly
chr15	40477831	G	A	BUB1B	NM_001211.5	p.Arg349Gln
chr15	40898643	G	C	KNL1	NM_170589.4	p.Arg43Thr
chr15	40903684	A	G	KNL1	NM_170589.4	p.Thr113Ala
chr15	40913840	G	T	KNL1	NM_170589.4	p.Ala486Ser
chr15	40914177	T	C	KNL1	NM_170589.4	p.Met598Thr
chr15	40915190	A	G	KNL1	NM_170589.4	p.Arg936Gly
chr15	40916237	A	G	KNL1	NM_170589.4	p.Lys1285Glu
chr15	40916801	A	G	KNL1	NM_170589.4	p.Thr1473Ala
chr15	74328116	A	G	PML	NM_033239.2	p.Ser772Gly
chr15	74328206	G	C	PML	NM_033239.2	p.Ala802Pro
chr15	74336633	T	C	PML	NM_033238.2	p.Phe645Leu
chr15	89876827	T	TTGC	POLG	NM_001126131.1	p.Gln53dup

Table S3: COSMIC Cancer Gene Census analysis of germline variants; related to Figure 1: The list of germline variants in annotated tumor suppressor genes (TSGs) by COSMIC Cancer Gene Census were also examined for the loss of sCNV status to identify any bi-allelic inactivated gene candidates. The sole germline variant with gnomAD allele frequency <= 0.1% in a loss sCNV segment (KMT2D p.Arg228Gly) was found to have lost the mutant allele, not the wild type allele. We therefore did not identify any functionally relevant, bi-allelic inactivated TSGs in the 2019 specimens.

Table S4

sample	Sample Type	Median Usable Calling Depth	Median Insert Size	Num Pf Clusters	Aligned Pf Reads Count	Aligned Pf Reads-Percent	Duplication Percent
normal-blood	normal	89	313	57,234,845	114,264,257	99.82	22.17
tumor-2016	tumor	230	254	193,039,303	385,778,108	99.92	39.23
tumor-A-Jun-2019	tumor	207	273	134,992,302	269,516,884	99.83	24.83
tumor-B-Jun-2019	tumor	184	289	122,795,895	245,068,214	99.79	24.88
tumor-Oct-2019	tumor	403	282	263,307,126	524,690,393	99.63	25.8
sample	**Target Bases Percent_1X**	**Target Bases Percent_10X**	**Target Bases Percent_20X**	**Target Bases Percent_30X**	**Target Bases Percent_40X**	**Target Bases Percent_50X**	**Target Bases Percent_60X**
normal-blood	99.05	98.43	97.77	96.92	95.4	91.95	85.29
tumor-2016	99.47	99.29	99.09	98.79	98.34	97.69	96.78
tumor-A-Jun-2019	99.09	98.63	98.28	97.95	97.62	97.29	96.9
tumor-B-Jun-2019	99.09	98.58	98.16	97.77	97.4	96.99	96.48
tumor-Oct-2019	99.15	98.88	98.77	98.69	98.62	98.56	98.5

Table S4: **Quality control metrics; related to Figure 1:** The sequencing QC metrics of tumor and matching normal patient specimens used in the study.

Table S5

Hairpins selected to target each gene, full hairpin sequences

	gene name	miR-1 flank 5' (21nt)	Variable Passenger (21nt)	Loop (18nt)	Variable Guide (21nt)	miR-1 flank 3' (21nt)
	generic	CCATATTCAGCCTTTGAGAGT	NNNNNNNNNNNNNNNNNNNNN	TAGTTATATTCAAGCATA	NNNNNNNNNNNNNNNNNNNNN	GCGAAATCTGGCGAGACATCG
cluster 012.1	*ft*	CCATATTCAGCCTTTGAGAGT	CTGGCTAAGTGTGGACAGAAA	TAGTTATATTCAAGCATA	TTTCTGTCCACACTTAGCCAG	GCGAAATCTGGCGAGACATCG
	kug	CCATATTCAGCCTTTGAGAGT	CAGAGGTTAAGTATAGGATAA	TAGTTATATTCAAGCATA	TTATCCTATACTTAACCTCTG	GCGAAATCTGGCGAGACATCG
	Xpd	CCATATTCAGCCTTTGAGAGT	CCCGAAGATACTCGATTTCGA	TAGTTATATTCAAGCATA	TCGAAATCGAGTATCTTCGGG	GCGAAATCTGGCGAGACATCG
cluster 012.2	*ft*	CCATATTCAGCCTTTGAGAGT	AACGGGTGAGGTGAAGACCAA	TAGTTATATTCAAGCATA	TTGGTCTTCACCTCACCCGTT	GCGAAATCTGGCGAGACATCG
	kug	CCATATTCAGCCTTTGAGAGT	ATCATGGGTGAACCATCAGAA	TAGTTATATTCAAGCATA	TTCTGATGGTTCACCCATGAT	GCGAAATCTGGCGAGACATCG
	Xpd	CCATATTCAGCCTTTGAGAGT	CCAGGTGACCATTTCGTCCAA	TAGTTATATTCAAGCATA	TTGGACGAAATGGTCACCTGG	GCGAAATCTGGCGAGACATCG

	gene name	
cluster 012.1	*ft*	CCATATTCAGCCTTTGAGAGTCTGGCTAAGTGTGGACAGAAATAGTTATATTCAAGCATATTTCTGTCCACACTTAGCCAGGCGAAATCTGGCGAGACATCG
	kug	CCATATTCAGCCTTTGAGAGTCAGAGGTTAAGTATAGGATAATAGTTATATTCAAGCATATTATCCTATACTTAACCTCTGGCGAAATCTGGCGAGACATCG
	Xpd	CCATATTCAGCCTTTGAGAGTCCCGAAGATACTCGATTTCGATAGTTATATTCAAGCATATCGAAATCGAGTATCTTCGGGGCGAAATCTGGCGAGACATCG
cluster 012.2	*ft*	CCATATTCAGCCTTTGAGAGTAACGGGTGAGGTGAAGACCAATAGTTATATTCAAGCATATTGGTCTTCACCTCACCCGTTGCGAAATCTGGCGAGACATCG
	kug	CCATATTCAGCCTTTGAGAGTATCATGGGTGAACCATCAGAATAGTTATATTCAAGCATATTCTGATGGTTCACCCATGATGCGAAATCTGGCGAGACATCG
	Xpd	CCATATTCAGCCTTTGAGAGTCCAGGTGACCATTTCGTCCAATAGTTATATTCAAGCATATTGGACGAAATGGTCACCTGGGCGAAATCTGGCGAGACATCG

Spacer sequences

spacer name	derived from	sequence
G-WAL F	vector	actctgaatagggaattgggaattgagatctgttctaga
G39.1	miR-1	agtagtgccaccaaaagttagccgcgttgtggaaaatcc
G39.2	miR-279	gagggaaatggagaacgcaaaaatcccattataatggaa
G39.4	miR-8	acaaataatgttgcaataaccagttgaaaccaatggaat
G-WAL R	vector	tagcggccgcaagaattcaggcgaga

Fully assembled cluster sequences

	GWAL-F	ft	G39.1	kug	G39.2	Xpd	G39.4	GWalR
012.1	actctgaatagggaa ttgggaattgagatc tgttctaga	CCATATTCAGCCTTTGAGAGTCT GGCTAAGTGTGGACAGAAATAGT TATATTCAAGCATATTTCTGTCCA CACTTAGCCAGGCGAAATCTGGC GAGACATCG	agtagtgccaccaaaagttagccgcgttg tggaaaatcc	CCATATTCAGCCTTTGAGA GTCAGAGGTTAAGTATAGG ATAATAGTTATATTCAAGCA TATTATCCTATACTTAACCT CTGGCGAAATCTGGCGAGA CATCG	gagggaaatggagaacgcaaaaatccc attataatggaa	CCATATTCAGCCTTTGAGAGTCC CGAAGATACTCGATTTCGATAGT TATATTCAAGCATATCGAAATCG AGTATCTTCGGGGCGAAATCTG GCGAGACATCG	acaaataatgt tgcaataacca gttgaaaccaa tggaat	tagcggccgc aagaattcag gcgaga
012.2	actctgaatagggaa ttgggaattgagatc tgttctaga	CCATATTCAGCCTTTGAGAGTAA CGGGTGAGGTGAAGACCAATAG TTATATTCAAGCATATTGGTCTTC ACCTCACCCGTTGCGAAATCTGG CGAGACATCG	agtagtgccaccaaaagttagccgcgttg tggaaaatcc	CCATATTCAGCCTTTGAGA GTATCATGGGTGAACCATC AGAATAGTTATATTCAAGC ATATTCTGATGGTTCACCCA TGATGCGAAATCTGGCGAG ACATCG	gagggaaatggagaacgcaaaaatccc attataatggaa	CCATATTCAGCCTTTGAGAGTCC AGGTGACCATTTCGTCCAATAGT TATATTCAAGCATATTGGACGAA ATGGTCACCTGGGCGAAATCTG GCGAGACATCG	acaaataatgt tgcaataacca gttgaaaccaa tggaat	tagcggccgc aagaattcag gcgaga
012.1	actctgaatagggaattgggaattgagatctgttctagaCCATATTCAGCCTTTGAGAGTCTGGCTAAGTGTGGACAGAAATAGTTATATTCAAGCATATTTCTGTCCACACTTAGCCAGGCGAAATCTGGCGAGACATCGagtagtgccaccaaaagttagccgcgttg							
012.2	actctgaatagggaattgggaattgagatctgttctagaCCATATTCAGCCTTTGAGAGTAACGGGTGAGGTGAAGACCAATAGTTATATTCAAGCATATTGGTCTTCACCTCACCCGTTGCGAAATCTGGCGAGACATCGagtagtgccaccaaaagttagccgcgttg							

Table S5: Construction of knockdown vectors; related to Figure 1. Sequences for the hairpin, spacer and assembled knockdown vectors are listed for CPCT012.1 and CPCT012.2. The assembled vector was then placed into a transformation vector as described in Materials and Methods.

Transparent Methods

Enrollment: This work was regulated by a biorepository protocol that managed specimen acquisition, processing and inventory and a separate protocol that governed analysis of genome data, model building validation and drug screening. Patient treatment was regulated by a third protocol and a personalized treatment consent written for the therapy recommended by the multidisciplinary tumor board. All protocols and consent forms were approved by the Mount Sinai Institutional Review Board.

Whole exome sequencing: Genome assays were performed on a fresh frozen tumor specimen and whole blood collected at the time of consent to serve as a patient matched normal (*i.e.* germline) control. Protocols for sample processing, genomic assays and analysis were as previously described (Uzilov *et al.*, 2016; Bangi *et al.*, 2019).

Paired-end (2×100 nt) whole exome sequencing (WES) was carried using Illumina HiSeq 2500 or 4000 instruments. Hybridization capture was carried out using SureSelect Human All Exon V5 (Agilent) for the 2016 specimen and Twist Human Core Exome for all three 2019 specimens. Libraries for tumor and normal samples were multiplexed in a 2:1 or 3:1 ratio of tumor to normal. The same normal (blood) sample was used as the matching normal for all four tumor specimens. Full details of the resulting sequencing QC result are given in Table S4.

Alignment of de-multiplexed FASTQ files and calling of molecular variants (somatic or germline SNVs and small insertions/deletions) were carried out using a Sema4 in-house pipeline (Tigris version 2.2.0). This pipeline implemented Broad Institute's best practices for running the Genome Analysis Toolkit (GATK) version 4.0.4.0 (McKenna *et al.*, 2010; DePristo *et al.*, 2011). The pipeline was written in Workflow Description Language (WDL) and executed using the Cromwell workflow engine using the Amazon AWS Batch backend. Sequencing reads were aligned to the hg19 human reference genome (*UCSC Genome Browser Downloads*, no date) using BWA-MEM version 0.7.17 (Li, 2013), duplicate reads were marked out using Picard MarkDuplicates (*Picard*, no date), and base quality recalibration was carried out using GATK4's BaseRecalibrator, resulting in BAM files used for all further analysis. Somatic mutations were called using GATK4's Mutect2 in tumor/normal analysis mode with default settings, then filtered using GATK4's FilterMutectCalls and FilterByOrientationBias. The resulting VCFs were loaded into a custom MySQL database schema using in-house scripts and annotated using RVS (Hakenberg *et al.*, 2016) and SnpEff 4.0b (Cingolani *et al.*, 2012), using the Ensembl version 75/GRCh37 resource bundle. The germline protein-altering variant KMT2D (p.Arg228Gly) was manually reviewed in IGV (Thorvaldsdóttir, Robinson and Mesirov, 2013) to inspect supporting alignment quality. Of note, the WES sequencing hybridization capture region was different in the 2016 specimen, and we could only apply GATK4 Somatic CNV to the 2019 specimens (Figure S1).

Somatic copy number variants (sCNV) calling and analysis: All 2016 and 2019 specimens were analyzed for sCNV using saasCNV (Zhang and Hao, 2015). In addition, since we have internal normal (blood) samples from other individuals sequenced via the same hybridization capture kit (Twist Human Core Exome) similar to the three 2019 specimens, we were able to create a panel of control samples; we therefore used GATK4 somatic CNV as an alternative sCNV calling tool to confirm the sCNV in all three 2019 specimens. NOTCH1 amplification was functionally confirmed by identifying nuclear-localized protein using immunohistochemical assays on tumor sections using previously described staining and scoring protocols (Donovan *et al.*, 2009; Bangi *et al.*, 2019)**.**

Model Building and Validation: In order to generate the patient model, a previously reported multigenic Drosophila transformation vector (Ni *et al.*, 2011; Bangi *et al.*, 2019) that contains three UAS cassettes was used. Each UAS cassette in the vector contains a unique multiple cloning site (MCS) flanked by a UAS promoter and SV40 transcription terminator sequence. The coding sequence for the truncated MYB protein observed in the patient was generated by PCR from a cDNA clone of the human MYB gene using the following forward and reverse primer sequences respectively: atgcGGCCGGCCcaaaATGGCCCGAAGACCCCG and atgcTTAATTAATTACTGCAAGGGGCTCGCCA. These primers also included restriction sites for enzymes FseI and PacI to the 5` and 3` ends of the product respectively, which were used to clone the amplified product into MCS1 of the multigenic vector (Figure 1D).

For gene knockdown, our previously established synthetic short hairpin cluster design where individual short hairpins were separated by spacer sequences found 5` to well expressed endogenous microRNAs in the Drosophila genome. Criteria for short hairpin selection and the protocol for short cluster design have both been previously reported (Vert *et al.*, 2006; Ni *et al.*, 2011; Bangi *et al.*, 2019). In order to increase the likelihood of success, two synthetic clusters that target the same three genes using different short hairpin sequences were designed (012.1 and 012.2). The hairpin, spacer and final cluster sequences can be found in Table S5. Cluster synthesis was outsourced to GENEWIZ. Sequence confirmed synthetic clusters 012.1 and 012.2 were separately cloned into a UAS cassette of the multigenic vector that already contained the truncated human MYB coding sequence using XbaI and NotI enzymes using restriction sites that were appended to the 5` and 3` ends of the clusters respectively. The UAS cassette that the clusters cloned into was specifically designed for short hairpin expression (Vert *et al.*, 2006; Ni *et al.*, 2011; Bangi *et al.*, 2019). The resulting two multigenic vectors both contained the same MYBΔC transgene and a different hairpin cluster targeting the same three genes using different hairpin sequences (Table S5).

After the final vectors were sequence confirmed, transgenic flies were generated by PhiC31-mediated targeted integration (Bischof *et al.*, 2007) into the second Drosophila chromosome using the landing site *attp40*. Tranegensis was outsourced to BestGene. After transgenic lines containing the multigenic vectors were generated, a previously established UAS-Notch line on chromosome three (Matsuno *et al.*, 2002) was introduced into the multigenic vector background to generate the final patient models: *w; UAS-multigenic [UAS-MYBΔC, UAS-3sh(Xpd,ft,kug)] attp40; UAS-N/S-T, Cy, Hu, Tb.*

The efficacy of gene knock-down induced by the hairpin clusters were evaluated by qPCR analysis. Experimental animals were generated by crossing patient models containing hairpin clusters 012.1 and 012.2 to a ubiquitously expressed *gal4* line that also contains a *gal80^{ts}* (*tub-gal4, tub-gal80^{ts}*) to transiently induce transgene expression for three days during larval development. Whole larvae with genotypes 1) *tub-gal4, tub-gal80^{ts}>UAS-012.1; UAS-N* 2) *tub-gal4, tub-gal80^{ts}>UAS-012.2; UAS-N*, and 3) *tub-gal4, tub-gal80^{ts}*/+ as controls were collected for RNA extraction (three biological replicates per genotype; six larvae per replicate) and stored in 300 µl RNALater (Life Technologies). For RNA extraction, Qiagen's RNeasy Plus Kit with RNase-free DNase Set for on-column DNA digestion was used following the manufacturer's instructions. RNA concentration was measured using Qubit. For qPCR analysis, 1 µg of RNA per replicate was used to generate complementary DNA (cDNA) using the High-Capacity RNA-to-cDNA kit (Life Technologies). qPCR assays were performed using the PerfeCTa SYBR Green FastMix for IQ (VWR Scientific). To identify the best housekeeping control, a panel of 5 candidate genes (*rpl32,*

hsp83, sdha, rpl13a and cyp33) were assayed. Of these, *rpl13a* produced the most robust and consistent result across replicates and genotypes and was selected as the housekeeping control. qPCR data were analyzed using the ΔΔC(t) method as previously described (Sopko *et al.*, 2014).

Quantifying *ptc>CPCT012*: Wing discs from wandering w^- (control) and *ptc>CPCT012* L3 larvae grown at 27 °C were fixed with 4% paraformaldehyde, mounted with Vectashield plus DAPI and imaged on a Leica DM5500 Q microscope. The same exposure (220 ms, 545 ms) and gain (2.8, 6.0) was used within each channel for all images. The *ptc* region was quantified using FIJI (ImageJ, v2.1.0) and represented as a ratio of the *ptc* region to total wing disc area to account for varying sizes of each individual wing disc. An outline was drawn around (i) the *ptc* region (GFP) or (ii) the entire wing disc (DAPI) manually using the freehand selection tool to exclude extraneous signal from the peripodial membrane, trachea, etc. Areas within the outlines were measured by establishing a threshold (*adjust→threshold*), then quantifying the GFP-labeled area (*analyze→analyze particles*). Area Ratios were calculated, graphed, and analyzed by Student's t-test (Microsoft Excel).

Drug Screening: Focused FDA Library was custom-made in house using drugs individually purchased as powder from Selleck Chemicals, LC Laboratories, TOcris Bioscience or MedChemExpress depending on availability. Stock solutions were made by dissolving drugs in water or 100% dimethyl sulfoxide (DMSO) at the highest possible concentration based on solubility information provided by the manufacturers. For each drug, the highest dose with no discernible toxicity (Maximum Tolerable Dose or MTD) on wildtype animals was selected for screening. Full FDA Library used for this patient was purchased from Selleck Chemicals in a 96-well format (100 µl of 10 mM solution). Both libraries were aliquoted into 384-well plates for screening. Drug screens were conducted at a single dose for each drug for both libraries along with DMSO and no DMSO controls (8 replicates per condition for Focused FDA screens and 4 replicates per condition for the Full FDA screens)

Drug-food was prepared using the PerkinElmer automated liquid handling workstation by mixing 0.7 µl of drug from the screening plate with 700 µl of semi-defined Drosophila medium (recipe available from the Bloomington Drosophila Stock Center) in 12 mm by 75 mm round-bottom test tubes (Sarstedt). As a result, each drug was diluted 1:1000 in the food, also bringing the DMSO concentration to 0.1% .

Drug food for combination screens were prepared by first adding 0.7 µl of 18 mM tofacitinib into each tube followed by 0.7 µl of each drug in the library and finally 700 µl Drosophila medium and mixing by repeated pipetting using the PerkinElmer automated liquid handling workstation, resulting in a 1:1000 dilution of each drug in the food and a DMSO concentration of 0.2%. Drug food for hit retests were prepared by hand, using a new batch of powder drug.

Experimental animals for drug screening were generated from the following cross: *w/Y; UAS-012.2; UAS-N X w; ptc-gal4, tub-gal80^{ts}* and directly aliquoted into the drug-food tubes as embryos after the food was solidified. Crosses were set up *en masse* in cages which produced embryos for four to five consecutive days laid on apple-juice plates supplemented with fresh yeast paste. Egg lays were performed at 22 °C for 24 hours to minimize transgene expression during embryogenesis and prevent embryonic lethality or irreversible developmental defects that could not be rescued by drug feeding during larval development.

Embryos were collected from fresh apple juice plates every day and embryo suspensions were generated in an "embryo buffer" designed to minimize embryo clumping and setting while aliquoting (15% glycerol, 1% Bovine

Serum Albumin, 0,1% Tween-20 in water). 7.5-10 µl embryo suspension was added to each drug-food tube using a single-channel, variable volume multi-dispense electronic pipette.

After the embryos were aliquoted, drug tubes were transferred to 29 °C to induce transgene expression. Tubes were scored for survival to adult stage 12 days later by counting both total number of experimental pupae (EP) and those that were empty, which reflected the number of experimental adults (EA). Drugs that showed significantly higher survival to the adult stage compared to controls based on multiple t tests (PRISM software) were considered hits.